In-situ high-energy X-ray diffraction and crystal plasticity modeling to predict the evolution of texture, twinning, lattice strains and strength during loading and reloading of beryllium

Ferreri, Nicholas Charles
Feng, Zhangxi
Savage, Daniel Jonathan
Brown, Donald William
Clausen, Bjorn
Sisneros, Thomas A.
Knezevic, Marko

To be published in: International Journal of Plasticity

DOI to publisher's version: 10.1016/j.ijplas.2022.103217

In-situ high-energy X-ray diffraction and crystal plasticity modeling to predict the evolution of texture, twinning, lattice strains and strength during loading and reloading of beryllium

Nicholas C. Ferreri[a], Zhangxi Feng[a], Daniel J. Savage[a,b], Donald W. Brown[b], Bjørn Clausen[b], Thomas A. Sisneros[b], Marko Knezevic[a,*]

[a]Department of Mechanical Engineering, University of New Hampshire, Durham, NH 03824, USA
[b]Materials Science & Technology Division, Los Alamos National Laboratory, Los Alamos, NM 87545, USA

Abstract

Deformation behavior of beryllium during compressive loading and cross-reloading is studied using *in-situ* high energy synchrotron X-ray diffraction microscopy and crystal plasticity modeling. The evolution of texture, twinning, elastic lattice strains, and flow stress are measured and compared with the predictions of an advanced elastic-plastic self-consistent (EPSC) crystal plasticity model. The model is initialized with the experimentally measured texture and residual stress produced by a simulation of cooling and calibrated to establish a set of model parameters using a portion of the measured data. The rest of the measured data is used for validation of the model. It is shown that the model is sufficiently flexible to reproduce the particularities pertaining to the complex strain-path-change and strain rate sensitive deformation of the material including the evolution of texture, twinning, lattice strains, transients in the stress-strain response, and anisotropic hardening with great accuracy using a single set of model parameters. From the comparison of the experimental data and predictions, we infer that the shifts in active deformation mechanisms between the slip systems from soft to hard and vice versa as well as between twinning to de-twinning are primarily responsible for drastic changes in the flow stress from one path to another. In particular, deformation twins form during compressive in-plane loading followed either by de-twinning during compressive cross-reloading in the through-thickness direction or by forming additional twin variants with some de-twinning of the existing variants during a compressive cross-reloading in another in-plane direction. The shifts in active deformation mechanisms are a consequence of changes in texture relative to the compression direction mediated with the deformation history and strain rate dependent dislocation density evolution governing hardening. The secondary effects improving the predictions come from accounting for residual stress, slip system-level backstress, and latent hardening.

Keywords: Texture; Twinning; Lattice strains; Crystal plasticity; HEDM; Beryllium

* Corresponding author at: University of New Hampshire, Department of Mechanical Engineering, 33 Academic Way, Kingsbury Hall, W119, Durham, New Hampshire 03824, United States. Tel.: 603 862 5179; fax: 603 862 1865.
E-*mail address*: marko.knezevic@unh.edu (M. Knezevic).

1. Introduction

Mg, Ti, Zr, Be are hexagonal close-packed (HCP) metallic materials receiving increasing interest for creating alloys for structural components, primarily because of their high strength-to-weight ratio. During manufacturing and often in-service, these metals undergo plastic deformation. As a result of plasticity, their microstructure and texture evolve changing their structural properties. The deformation of HCP metals is carried out by multiple deformation mechanisms i.e. prismatic, basal, and pyramidal slip, and deformation twinning. The relative contribution of these deformation mechanisms to the plasticity depends on crystallographic texture with respect to the straining direction, as well as strain rate and temperature of deformation (Christian and Mahajan, 1995; Yoo, 1981). For example, increased strain rate and decreased temperature suppress the thermally-activated dislocation glide, while increasing the activity of deformation twinning (Knezevic et al., 2013a; Knezevic et al., 2015; Song and Gray, 1995). Moreover, shifts in the relative activities of slip and twinning deformation mechanisms due to new slip systems and twin variants activating and/or prior slip system reversing the glide direction and/or twin domains shrinking (de-twinning) occur during strain-path changes. These basic sub-grain-scale processes govern the flow stress response in addition to the concomitant microstructural evolution (Brown et al., 2012; Sisneros et al., 2010).

Microstructure-sensitive models capable of predicting how the thermo-mechanical response of crystalline materials is affected by their microstructure and local intrinsic anisotropic constitutive behavior have been the subject of intensive research for several decades. A number of models have been developed ranging from Taylor-type upper-bound (Fromm et al., 2009; Knezevic et al., 2009; Knezevic et al., 2008; Knezevic and Savage, 2014; Taylor, 1938), mean-field self-consistent (SC) (Feng et al., 2021; Knezevic et al., 2013b; Knezevic et al., 2016b; Lebensohn and Tomé, 1993; Turner and Tomé, 1994) to spatially resolved such as crystal plasticity finite element (Ardeljan et al., 2014; Ardeljan et al., 2015a; Ardeljan et al., 2016b; Kalidindi et al., 1992; Knezevic et al., 2014; Knezevic et al., 2010; Roters et al., 2010) and Green's function fast Fourier transform formulations (Eghtesad et al., 2018a; Eghtesad et al., 2020; Eghtesad and Knezevic, 2020a, b, 2021; Eghtesad et al., 2018d; Lebensohn et al., 2012). While the spatial models can be used for detailed simulations accounting for grain-to-grain interactions, the Taylor-type and SC models are more computationally efficient and have proven effective in predicting the homogenized flow stress and texture evolution of polycrystals. Another important advantage of these models is in the schemes for handling deformation twinning, while the explicit incorporation of twinning in the spatial models is challenging (Ardeljan et al., 2017; Ardeljan and Knezevic, 2018; Ardeljan et al., 2015b; Knezevic et al., 2016a). Additionally, the Taylor-type and SC crystal plasticity models can serve as constitutive laws in the finite element method (FEM) simulations (Jeong et al., 2021; Knezevic et al., 2013c; Prakash et al., 2015; Segurado et al., 2012; Tomé et al., 2001; Walde and Riedel, 2007; Zecevic et al., 2016a; Zecevic and Knezevic, 2018b; Zecevic et al., 2021). In such formulations, the spatial variation in deformation from point to point across the FE model relaxes the intrinsic homogenization assumptions (Ardeljan et al., 2016a; Feather et al., 2019; Feather et al., 2021). The development and validation of such material models with sensitivity to microstructure and its evolution is critical for engineering analysis and material design, especially with the advent of high-performance computing for materials science applications (Eghtesad et al., 2018c; Eghtesad et al., 2020; Eghtesad and Knezevic, 2018; Panchal et al., 2013). Modeling the complex deformation behavior of HCP metals requires such sophisticated models based on crystal plasticity theory to link crystallographic deformation mechanisms and texture evolution to highly anisotropic material properties (Kocks et al., 1998).

The activation of deformation mechanisms in crystal plasticity models is controlled by crystallography of grains relative to the sense of loading and by a set of model parameters determining the resistance to slip/twin. These model parameters are calibrated using stress–strain curves for a material through a fitting procedure (Savage et al., 2021). Data such as elastic lattice strains and geometrical changes upon deformation are used for verification of the parameters. Moreover, microstructural data such as the evolution of texture and twinning provide further verification. The advent of techniques such as high-energy synchrotron X-ray diffraction microscopy allows for the unprecedented ability to collect *in-situ* polycrystalline microstructural evolution data for detailed calibration and validation of crystal plasticity models (Poulsen, 2004; Shade et al., 2019; Wang et al., 2014). Specifically, the high energy and brightness of synchrotron X-rays enables detailed probing of the internal structure within bulk samples during *in-situ* loading/unloading. An X-ray exposure that probes a given volume of a polycrystal produces reflections for all sampled grains that meet the Bragg diffraction criteria. These grains have different neighborhoods and average the diffraction signal. From these reflections, information on crystallographic interplanar spacing (d-spacing), crystallite size (size of diffracting volume/crystallite), and crystallographic texture can be inferred. When a series of X-ray exposures is collected from a deforming polycrystalline sample, the evolution of the mean d-spacing for a given diffracting plane is observed to shift due to the uniform intragranular lattice strains associated with elastic deformation. If polycrystalline samples are deformed beyond yield, *in-situ* X-ray exposures would show diffraction patterns with broadening reflections, which result from plasticity-induced, non-uniform lattice strains (micro-strain). Elasto-plastic (EP) SC models have been used to interpret lattice strain and macroscopic stress-strain data from these types of *in-situ* experiments (Clausen et al., 2008; Wollmershauser et al., 2012; Zecevic et al., 2015). Specifically, these models and the corresponding *in-situ* diffraction measurements probe their respective polycrystalline samples in similar ways, which facilitates model validation.

Models are typically developed and tested in monotonic deformations applied in one direction, whereas in practice, metals usually experience frequent changes in strain paths, strain rates, and temperatures. In order to predict the mechanical response and microstructural evolution of HCP metals during a sequence of two or more strain paths such as compression in one direction under one strain rate to a given strain level and then compression in a perpendicular direction under a different strain rate, the model must account for phenomena such as residual stress, backstress, reverse glide of mobile dislocations, and de-twinning (Kitayama et al., 2013a; Knezevic et al., 2013a; Peeters et al., 2001; Proust et al., 2010; Rauch et al., 2011; Wen et al., 2015a; Wen et al., 2016). The present work is concerned with *in-situ* high-energy X-ray diffraction and crystal plasticity modeling of deformation characteristics during loading and reloading of Be, a material much less studied than other HCP metals (Abey, 1970; Blumenthal et al., 2004; Brown et al., 2005b; Kokovikhin et al., 1990).

A recently developed multi-scale (MS) EPSC model (Zecevic et al., 2015) incorporated several grain- and sub-grain-level models: the dislocation density-based hardening law (Beyerlein and Tomé, 2008; Brown et al., 2012), the composite grain (CG) twinning model (Proust et al., 2007) improved to nucleate multiple twin domains/twin variants within the same grain, stress fluctuations to influence twin nucleation (Niezgoda et al., 2014) and de-twinning. The work presented here advances the MS-EPSC model for HCP metals to account for slip system-level backstress, dissolution of dislocations upon strain-path-change, and latent hardening. While the first phenomenon is important for predicting re-yielding i.e. the Bauschinger effect (BE), the latter two phenomena are important for predicting change in the hardening rates upon reloading. The advanced MS-EPSC model is applied to a comprehensive set of data involving flow stress, texture, twin volume fraction, and lattice strains recorded during fourteen tests each involving a loading path followed by a cross-reloading path in compression under different strain rates. While reproducing the data, the model adjusts the relative activity of slip-dominated deformation for some strain paths, while slip and de-twinning or slip, twinning, and de-twinning for other deformation paths. Remarkably, the model predicts the role of shifts in slip, twinning, and de-twinning on the change in yield and flow stresses upon reloading at variable strain rates. Good agreement in predicting the evolution texture, twin fraction in twinning and de-twinning is also achieved in every strain path. Finally, the evolution of elastic lattice strains compare well with the data measured by means of *in-situ* high-energy x-ray diffraction during compressive loading and unloading. Furthermore, the essential effects of residual stresses, backstress, and reverse dislocation glide on the mechanical response during loading and reloading are predicted and discussed.

2. Experimental methods

2.1 Material and sample preparation

The Be used in this study was a rolled plate of 4.8 mm thickness by approximately 0.5 m wide and 2 m long. More details about processing of the plate can be found in (Brown et al., 2013). A set of samples, rectangular prisms with dimensions 2.5 mm x 2.5 x mm x 4.0 mm, were cut from the plate using electro-discharge machining (EDM). Sample orientation with respect to the frame of the Be plate is shown in Fig. 1a: in-plane axes IP1 and IP2 are the rolling and transverse directions, while through thickness (TT) is the plate normal direction. These samples were used for mechanical testing along different sample directions.

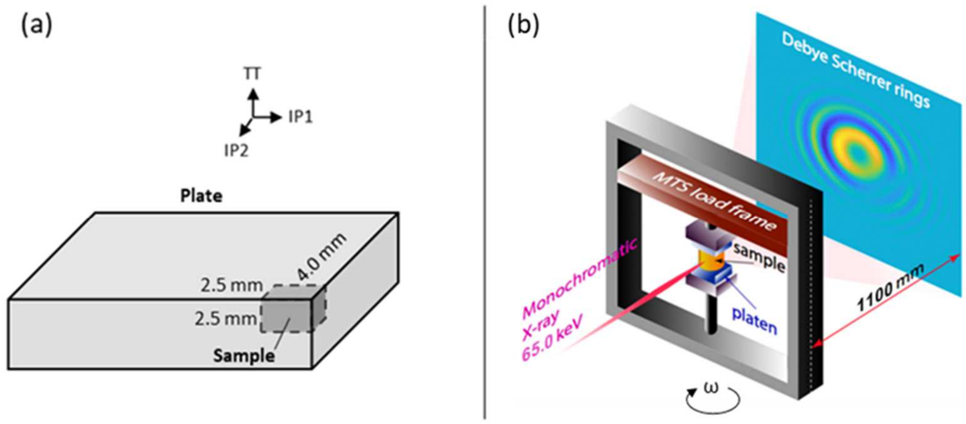

Figure 1. (a) Sample orientation with respect to the frame of the Be plate: in-plane axes IP1 and IP2 are the rolling and transverse directions, while through thickness (TT) is the plate normal direction. (b) A schematic of the APS 1-ID-E experimental apparatus for collecting X-ray diffraction measurements during *in-situ* loading. The apparatus integrates an MTS servo-hydraulic load frame with dies holding a sample. A compressive force is applied on the sample while allowing unobstructed paths for the incident high-energy monochromatic X-rays and outgoing diffracted X-rays.

2.2 Quasi-static and Split-Hopkinson pressure bar and compressive pre-loading

Ten samples were pre-strained *ex-situ* in compression for subsequent *in-situ* reloading along with X-ray diffraction measurements of lattice strains and texture. Four samples were compressed along IP1 to different pre-strain levels at room temperature under a strain rate of 10^{-3} s^{-1} in an Instron load frame dedicated to the Spectrometer for Materials Research at Temperature and Stress (SMARTS), the Lujan Center, LANSCE, Los Alamos National Laboratory (Bourke et al., 2002). Six samples were compressed along IP1 to different pre-strain levels at room temperature under a strain rate of 2000 s^{-1} using a Split-Hopkinson Pressure Bar (Chen and Kocks, 1991; Follansbee, 1985). Table 1 summarizes the tests performed on these 10 samples of Be (A-J). Data for the samples K-L is taken from prior works involving the same material (Brown et al., 2013). A total of fourteen preload specimens to variable strain levels under variable strain rates (0.001 s^{-1}, 5 s^{-1} and 2000 s^{-1}) is aimed to study mechanical response and microstructural change transients in subsequent reloading.

Table 1: Compressive strain path change mechanical tests performed on samples of Be.

Case	Preload axis (strain rate)	True strain	Reload axis (strain rate)	Additional true strain
A	IP1 (0.001 s^{-1})	0.165	TT (0.0002 s^{-1})	0.0785

B	IP1 (0.001 s^{-1})	0.095	TT (0.0002 s^{-1})	0.0584
C	IP1 (0.001 s^{-1})	0.058	TT (0.0002 s^{-1})	0.0635
D	IP1 (2000 s^{-1})	0.144	TT (0.0002 s^{-1})	0.0934
E	IP1 (2000 s^{-1})	0.064	TT (0.0002 s^{-1})	0.0597
F	IP1 (2000 s^{-1})	0.1	TT (0.0002 s^{-1})	0.071
G	IP1 (2000 s^{-1})	0.203	IP2 (0.0002 s^{-1})	0.1
H	IP1 (0.001 s^{-1})	0.173	IP2 (0.0002 s^{-1})	0.116
I	IP1 (2000 s^{-1})	0.066	IP2 (0.0002 s^{-1})	0.098
J	IP1 (2000 s^{-1})	0.097	IP2 (0.0002 s^{-1})	0.104
K	IP1 (5 s^{-1})	0.22	TT (5 s^{-1})	0.15
L	IP1 (5 s^{-1})	0.22	TT (0.001 s^{-1})	0.15
M	IP1 (5 s^{-1})	0.22	IP2 (5 s^{-1})	0.15
N	IP1 (5 s^{-1})	0.22	IP2 (0.001 s^{-1})	0.15

2.2 High-energy X-ray diffraction experiments

In-situ X-ray diffraction experiments were performed at the Advanced Photon Source (APS) 1-ID-E beamline, Argonne National Laboratory. The schematic of the *in-situ* experimental setup is shown in Fig. 1b. The X-ray energy was 65.0 keV (wavelength of 0.01907 nm) and the sample to detector distance was 1100 mm. The instrument was calibrated using a standard CeO_2 specimen (Kaiser and Watters Jr, 2007). Monotonic, displacement-controlled compression tests were carried out at room temperature at a strain rate of $2x10^{-4}$ s^{-1} using an MTS servo-hydraulic load frame. The *is-situ* loading was performed without a need for holding time. The wide angle X-ray scattering (WAXS) data were collected on a single a GE 41RT area detector (Shastri et al., 2002) with 2048 x 2048 pixels (0.2×0.2 mm^2 pixel size). Both the WAXS and the MTS load frame data acquisition rates were aligned, making it possible to obtain WAXS data as a function of sample displacement or applied load. For these tests, the rectangular parallelepiped samples preloaded along the IP1 direction were reoriented by 90° and subjected to *in-situ* reloads either along TT (six samples) or IP2 (four samples). For TT reloads, the IP2 sample axis was transverse to the straining direction, and the original straining direction (IP1) was the second transverse direction. For IP2 reloads, the TT sample axis was transverse to the straining direction, and the original straining direction (IP1) was also the second transverse direction. When strained along TT or IP2 during reloading, incident X-rays entered the sample along IP1. These complex experiments are designed to provide data for the interpretation of the interactions between slip and twinning/de-twinning and the mechanisms underlying unloading, BE, transients in strength, and subsequent hardening.

Ex-situ X-ray diffraction experiments were also performed at the APS 1-ID-E beamline for texture. The experimental setup was similar to the *in-situ* setup with the primary exception being that the sample to detector distance was reduced to 680 mm, reducing the resolution but increasing the number of hkl's observed and improving texture analysis. Each *ex-situ* experiment consisted of 8 separate X-ray exposures, which were collected with the sample rotated at different angles (ω = -10°, 0°, 10°, 20°, 30°, 40°, 50°, and 60°) about the loading axis. An *ex-situ* experiment for texture analysis was performed once before reloading and once after unloading.

3. Data analysis

3.1 Calculating lattice strains

A step-by-step guide to the lattice strain analysis performed in GSAS-II using in-situ X-ray diffraction data is provided in Appendix A, and only a brief description of the procedure exists here. To ensure accurate lattice strain calculations for Be samples, instrument parameters were calibrated in GSAS-II using data collected from the CeO_2 standard sample. Once calibrated, regions of the two-dimensional WAXS Be diffraction patterns were isolated for analysis. Fig. 2a shows the vertical slices in a Be diffraction image that correspond to diffracting planes with poles approximately parallel to the loading axis, and the horizontal slices corresponding to diffracting planes with poles approximately perpendicular to loading. The arclength of these slices is 15°η (i.e. 7.5° around the loading axis for the vertical arc, while the same around the horizontal axis for the horizontal arc). Horizontal and vertical slices were integrated and averaged separately to convert the 2D image data into 1D intensity vs. d-spacing histograms (Toby and Von Dreele, 2013). This process, once initialized for a sample, was automatically applied to all diffraction images in the dataset. The histograms corresponding to a single X-ray exposure taken before and after *in-situ* loading are shown in Fig. 3a,b and 3c,d, respectively. Furthermore, the histograms in Fig. 3a,c represent diffracting planes with poles perpendicular to loading and the histograms Fig. 3b,d represent diffracting planes with poles parallel to loading. 5 Be reflections were captured ($\{10\bar{1}0\}$, $\{0002\}$, $\{10\bar{1}1\}$, $\{10\bar{1}2\}$, and $\{11\bar{2}0\}$). These peaks were fit in GSAS-II, 2θ values were converted to d-spacing, and lattice strains were calculated using the method discussed in (Brown et al., 2003). The reference d-spacing for lattice strain calculations was measured from an uncompressed sample of Be that originated from the same plate as other samples. Consequently, the calculated lattice strains are with respect to the hot-pressed and machined state of the uncompressed sample. Therefore, since the calculated lattice strains do not account for thermal residual strains left from the processing of the plate, they should be referred to as mechanically-induced lattice strains (Brown et al., 2003).

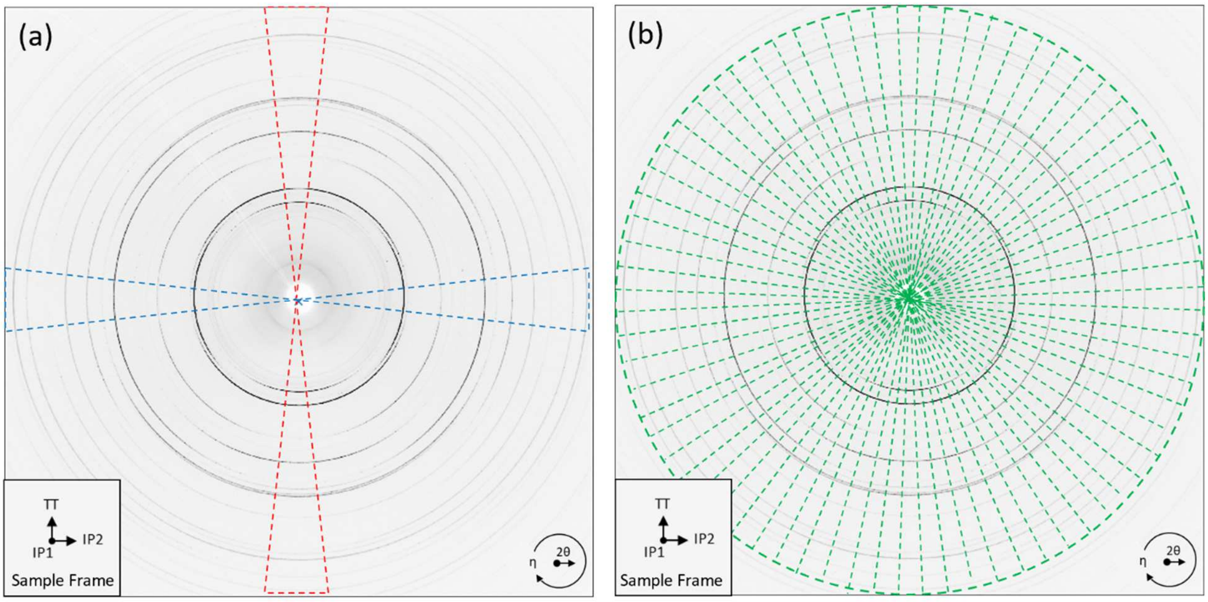

Figure 2: (a) High-energy X-ray diffraction pattern of sample B during *in-situ* loading that shows integration regions for lattice strain analysis. Areas outlined in red highlight diffracting planes with poles that are parallel to the loading axis, and areas outlined in blue highlight diffracting planes with poles perpendicular to loading. Incident X-rays are along IP1. (b) High-energy X-ray diffraction pattern of sample B during *in-situ* loading that shows integration regions for texture analysis. Incident X-rays are along IP1.

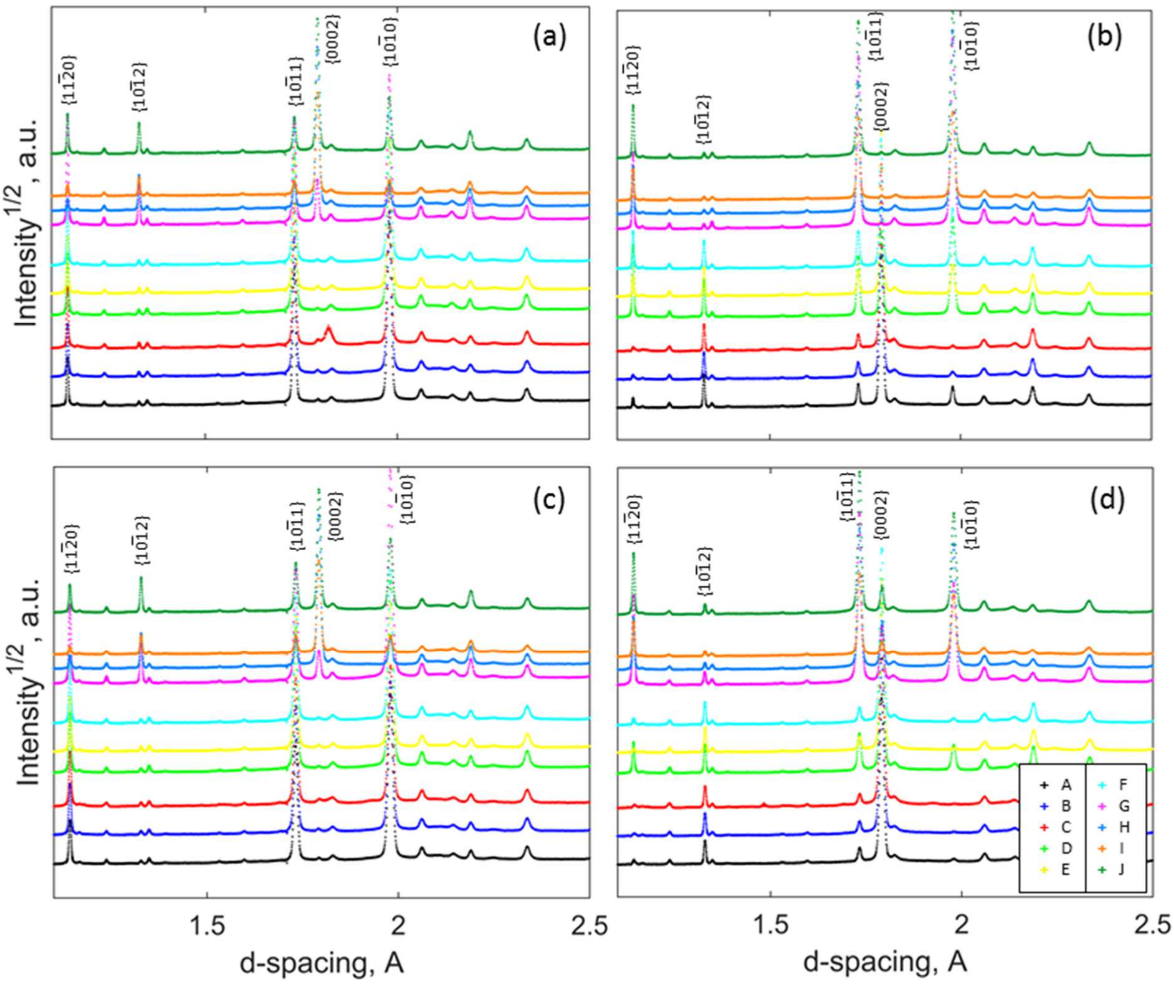

Figure 3: Histograms created by integrating horizontal and vertical slices of a diffraction pattern collected (a,b) before and (c,d) after *in-situ* loading. The horizontal and vertical slices of the diffraction pattern that were integrated represent diffracting planes with poles (a,c) perpendicular and (b,d) parallel to loading, respectively. Five Bragg reflections are observed for metallic Be, and peaks from various Be oxides can also be seen (especially at higher d-spacings). Be oxides is approximately 2%.

3.2 Calculating crystallographic texture

A step-by-step guide to the texture analysis performed in Maud using *ex-situ* X-ray diffraction data is provided in Appendix A, and only a summary is given in this section. The Maud diffraction analysis software was used to convert all X-ray diffraction images collected for texture analysis into histograms, which were then analyzed. The models governing the calculated diffraction histograms in Maud are described in references (Alves et al., 2015; Matthies et al., 1997; Wenk et al., 2003) and incorporate effects of sample geometry, instrumentation, and material structure on the intensity and shape of Bragg reflections.

The 8 diffraction images corresponding to the 8 sample rotation angles (ω) at which X-ray exposures were taken were binned into 72 regions (with arclengths of 5°Φ), each of which was integrated and converted into a 1D intensity vs. d-spacing histogram. The Rietveld method was applied whereby the relevant crystallographic and scaling parameters were refined to increase the quality of the least-squares fit between calculated and experimental diffraction histograms. An orientation distribution function (ODF) was calculated from the 576 histograms, which provide intensity data on all diffracting planes as a function of ω and Φ angles. The Rietveld refinement method used for texture analysis in Maud is based on the work in (Wenk et al., 2010).

3.3 Calculating twin volume fractions from crystallographic texture

Since no spatial characterization of the material was possible, twin volume fractions were estimated after characterizing texture evolution as the volume fraction of crystal orientations with **c**-axis close to the compression direction (Bhattacharyya et al., 2016; Brown et al., 2005a; Feather et al., 2019; Jain and Agnew, 2007). The underlying assumption is that tensile twins reorient texture strictly toward the compression direction and there is minimal reorientation due to slip induced lattice spin. A misorientation cutoff angle of 30° between the compression direction and **c**-axis was utilized to identify the twin volume fraction per sample after deformation. The method does not account for any secondary twins, which may develop in primary twins.

4. Modeling framework

The deformation behavior of Be is modeled using a recently developed MS-EPSC (Zecevic et al., 2015), which incorporates several sub-models: the dislocation density-based hardening law (Beyerlein and Tomé, 2008), the composite grain (CG) twinning model (Proust et al., 2007) improved to nucleate multiple twin domains/twin variants within the same grain, stress fluctuations influencing twin nucleation (Niezgoda et al., 2014) and de-twinning. Specifically for modeling of strain-path-change deformation of Be, the model is improved to account for dissolution of dislocations upon reloading, slip system-level backstress, and latent hardening, taking advantages of the work presented in (Barrett et al., 2020). Combining these sub-models into one advanced version of MS-EPSC enables modeling of strain-path and strain rate sensitive deformation of the highly anisotropic response of Be. A summary of the modelling framework is presented next.

In the description that follows, " $\cdot$ " represents the dot product, while " $\otimes$ " represents the tensor product. Also, bold letters are used for tensors, while tensor components and scalars are italic but not bold. A family of slip systems (slip mode) is denoted with "α", while an individual slip system belonging to a family is denoted with "s". Moreover, the notation distinguishes between positive $s+$ and negative $s-$ slip system directions for every s. Likewise, a twin mode is denoted with "β" and twin systems with "t".

In SC modeling, the polycrystalline material is represented using a set of ellipsoids, where each ellipsoid is a grain, which is treated as an elasto-plastic inhomogeneity embedded in a homogenous-effective-medium (HEM). The inhomogeneity inclusion interacts with the HEM in an average sense (Lipinski and Berveiller, 1989; Zecevic and Knezevic, 2019). The averaged rate of Jaumann stress and strain rate over constituent grains is that of the HEM: $\hat{\boldsymbol{\sigma}} = \langle \hat{\boldsymbol{\sigma}}^c \rangle$ and $\dot{\boldsymbol{\varepsilon}} = \langle \dot{\boldsymbol{\varepsilon}}^c \rangle$ (Neil et al., 2010). $\langle \quad \rangle$ denotes volume average. The following linearization relations are employed to relate overall- (polycrystal-) and grain-level (the superscript "*c*" denotes grain- or crystal-level) constitutive quantities

$$\hat{\boldsymbol{\sigma}} = \mathbf{L}\dot{\boldsymbol{\varepsilon}}, \tag{1}$$

$$\hat{\boldsymbol{\sigma}}^c = \mathbf{L}^c \dot{\boldsymbol{\varepsilon}}^c, \tag{2}$$

The rate of Cauchy stress can be readily obtained from the rate of Jaumann stress using $\dot{\boldsymbol{\sigma}} = \hat{\boldsymbol{\sigma}} + \langle \mathbf{W}^c \boldsymbol{\sigma}^c \rangle - \langle \boldsymbol{\sigma}^c \mathbf{W}^c \rangle = \mathbf{L}\dot{\boldsymbol{\varepsilon}} + \langle \mathbf{W}^c \boldsymbol{\sigma}^c \rangle - \langle \boldsymbol{\sigma}^c \mathbf{W}^c \rangle$. In this relationship, $\mathbf{W}^c$ is the grain *c* spin tensor. The overall and grain strain rates are related through a localization tensor, $\mathbf{A}^c$

$$\dot{\boldsymbol{\varepsilon}}^c = \mathbf{A}^c \dot{\boldsymbol{\varepsilon}}. \tag{3}$$

The localization tensor $\mathbf{A}^c$ is calculated based on an instantaneous grain-level elasto-plastic stiffness, $\mathbf{L}^c$, and that of the polycrystal, $\mathbf{L}$,

$$\mathbf{A}^c = \left(\mathbf{L}^c + \mathbf{L}^{c^*}\right)^{-1}\left(\mathbf{L}^{c^*} + \mathbf{L}\right) \text{ with } \mathbf{L}^{c^*} = M_{eff}\mathbf{L}(\mathbf{S}^{c^{-1}} - \mathbf{I}). \tag{4}$$

In Eq. (4), $\mathbf{L}^{c^*}$ is the effective stiffness governing the interaction between the grain and overall quantities: $(\hat{\boldsymbol{\sigma}}^c - \hat{\boldsymbol{\sigma}}) = -\mathbf{L}^{c^*}(\dot{\boldsymbol{\varepsilon}}^c - \dot{\boldsymbol{\varepsilon}})$, $\mathbf{S}^{c^{-1}}$ is the symmetric Eselby tensor (Eshelby, 1957), and $\mathbf{I}$ is the 4$^{\text{th}}$ rank identity tensor. The parameter M_{eff} can be used to tune strength of the interaction between inclusions and HEM (Savage et al., 2019; Tomé, 1999) but is set to 1 in the present work. Finally, $\mathbf{L}$ becomes $\mathbf{L} = \langle \mathbf{L}^c \mathbf{A}^c \rangle \langle \mathbf{A}^c \rangle^{-1}$.

The constitutive relation at the grain-level is: $\hat{\boldsymbol{\sigma}}^c = \mathbf{C}^c\left(\dot{\boldsymbol{\varepsilon}}^c - \boldsymbol{\alpha}^c \dot{T} - \sum_s \mathbf{m}^{c,s}\dot{\gamma}^{c,s}\right) - \boldsymbol{\sigma}^c tr(\dot{\boldsymbol{\varepsilon}}^c)$. Then, the grain-level instantaneous stiffness is

$$\mathbf{L}^c = \mathbf{C}^c - \mathbf{C}^c \sum_s \mathbf{m}^{c,s} \otimes \left(\sum_{s'} \left(X^{ss'}\right)^{-1} \mathbf{m}^{c,s'} \left(\mathbf{C}^c - \boldsymbol{\sigma}^c \otimes \mathbf{i}\right)\right) - \boldsymbol{\sigma}^c \otimes \mathbf{i}\,, \tag{5}$$

where

$$X^{ss'} = h^{ss'} + h_{bs}^{ss'} + \mathbf{C}^c \cdot \mathbf{m}^{c,s} \otimes \mathbf{m}^{c,s'}. \tag{6}$$

In the above equations, $\mathbf{C}^c$ is the grain-level elasticity tensor calculated based on the single crystal elastic constants and crystallographic orientation and $\mathbf{m}^{c,s} = \frac{1}{2}(\mathbf{b}^{c,s} \otimes \mathbf{n}^{c,s} + \mathbf{n}^{c,s} \otimes \mathbf{b}^{c,s})$ is the Schmid tensor for slip system *s*. The unit Burgers vector, $\mathbf{b}^{c,s}$, and plane normal, $\mathbf{n}^{c,s}$, are the geometry of slip system, *s*. In Eq. (6), $h^{ss'}$ and $h_{bs}^{ss'}$ are the hardening matrix and the back-stress matrix, respectively. Expressions for these matrices are defined based on a hardening law and a back-stress law as derivatives with respect to the shear rate, $\dot{\gamma}^s$: $h^{ss'} = \frac{\partial \tau_c^s}{\partial \gamma^{s'}}$, $h_{bs}^{ss'} = \frac{\partial \tau_{bs}^s}{\partial \gamma^{s'}}$

(Ghorbanpour et al., 2020; Ghorbanpour et al., 2017; Zecevic and Knezevic, 2018a; Zecevic et al., 2019b):. The laws are described below.

For the activity of a deformation system, two conditions are: (1) $\mathbf{m}^{c,s} \cdot \boldsymbol{\sigma}^{c} - \tau_{bs}^{c,s} = \tau_{c}^{c,s}$ and (2) $\mathbf{m}^{c,s} \cdot \dot{\boldsymbol{\sigma}}^{c} - \dot{\tau}_{bs}^{c,s} = \dot{\tau}_{c}^{c,s}$, where $\tau_{bs}^{c,s}$ is the slip system backstress and $\mathbf{m}^{c,s} \cdot \widehat{\boldsymbol{\sigma}}^{c}$ is the shear stress resolved on the slip system. The conditions imply that the shear stress resolved on the system after the backstress correction must be on the yield surface and must remain on it as it evolves. The evolution laws for slip and twin resistances drive the evolution of the crystal yield surfaces. The kinematic effects at the system level are introduced by backstress. Therefore, the crystal yield surfaces for slip evolve with deformation through the slip resistance, $\tau_{c}^{c,s}$, and shifts through the backstress, $\tau_{bs}^{c,s}$. The resistance and backstress terms evolve with the shear rates using

$$\dot{\tau}_{c}^{c,s} = \sum_{s'} h^{ss'}\, \dot{\gamma}^{c,s'}, \dot{\tau}_{bs}^{c,s} = \sum_{s'} h_{bs}^{ss'}\, \dot{\gamma}^{c,s'}. \tag{7}$$

The spin tensor per grain, *c*, is

$$\mathbf{W}^{c} = \mathbf{W} + \boldsymbol{\Pi}^{c} - \mathbf{W}^{p,c}, \tag{8}$$

where $\mathbf{W}$ is an imposed spin over the polycrystal, $\boldsymbol{\Pi}^{c}$ is the antisymmetric Eshelby tensor (Lebensohn and Tomé, 1993), and $\mathbf{W}^{p,c} = \sum_{s} \mathbf{q}^{c,s}\dot{\gamma}^{c,s}$ is the plastic spin with $\mathbf{q}^{c,s} = \frac{1}{2}(\mathbf{b}^{c,s} \otimes \mathbf{n}^{c,s} - \mathbf{n}^{c,s} \otimes \mathbf{b}^{c,s})$.

4.1 Deformation history dependent hardening law

The dislocation density-based hardening law advanced in the present work was originally developed for HCP Zr in (Beyerlein and Tomé, 2008) and then used for other HCP metals including Be (Ardeljan et al., 2015a; Knezevic et al., 2013a). According to this law formulation, the resistance to slip, τ_{c}^{α}, consists of the initial slip resistance, τ_{0}^{α}, which is thought to represent the Peierls stress and the initial density of dislocations; the Hall-Petch-like barrier term due to presence of twins, τ_{HP}^{s}, which is dependent on the mean free path distance reduced from the grain size by the presence of twins; the strain rate and temperature sensitive resistance due to forest dislocation density, τ_{forest}^{s}; and the strain rate and temperature sensitive resistance due to dislocation debris, τ_{deb}^{α}

$$\tau_{c}^{s}(\dot{\varepsilon}, T) = \tau_{0}^{\alpha} + \tau_{HP}^{s} + \tau_{forest}^{s}(\dot{\varepsilon}, T) + \tau_{deb}^{\alpha}(\dot{\varepsilon}, T). \tag{9}$$

The initial value is fitted, while the remaining terms are calculated using

$$\tau_{0,HP}^{\alpha} = \mu^{\alpha} HP^{\alpha} \sqrt{\frac{b^{\alpha}}{d_g}}, \tag{10a}$$

$$\tau_{forest}^{s} = b^{\alpha}\chi\mu^{\alpha}\sqrt{\sum_{s'} L^{ss'}\rho_{tot}^{s'}}, \tag{10b}$$

$$\tau_{deb}^{\alpha} = 0.086\, \mu^{\alpha} b^{\alpha}\sqrt{\rho_{deb}}\,log\left(\frac{1}{b^{\alpha}\sqrt{\rho_{deb}}}\right). \tag{10c}$$

Therefore, the assumed additive decomposition of slip resistance represents the actual physical background and facilitate the formulation of hardening through the evolving terms. In Eq. (1), χ

is a dislocation interaction parameter usually set to 0.9 (Lavrentev, 1980; Zecevic and Knezevic, 2018a), ρ_{tot}^{s} is the slip system level total forest density of dislocations, ρ_{deb} is the debris dislocation density, μ^{α} is the shear modulus per slip mode, b^{α} is the Burgers vector per mode, and $L^{ss'}$ includes a set of latent hardening constants.

While the Hall–Petch-like barrier hardening effect due to grain size, $\tau_{0,HP}^{\alpha}$, is included in the initial slip resistance, such hardening arises additionally from subdivision of grain due to twinning. The barrier effect due to twinning is formulated as (Knezevic et al., 2015)

$$\tau_{HP}^{s} = \frac{f^{PTS} - f^{PTS,0}}{f^{PTS,max} - f^{PTS,0}} \mu^{\alpha} HP^{\alpha} \sqrt{\frac{b^{\alpha}}{d_{mfp}^{s}}}, \tag{11}$$

where $d_{mfp}^{s} = \frac{(1-f^{PTS})d_c}{\sin(\lambda)}$ is the mean-free-path. Here, λ is the angle formed by the slip plane and the plane of the twin. The latter plane is that of a selected predominant twin system (PTS) if multiple twin variants form in the given grain. The remaining constant, $d_c = \frac{d_g}{n^{lamellas}}$, is the distance between twin lamellae calculated using the grain size, and a chosen number of lamella developing per grain, $n^{lamellas}$, which is taken to be 4. The barrier factor (BF), $\frac{f^{PTS} - f^{PTS,0}}{f^{PTS,max} - f^{PTS,0}}$ includes two constants, $f^{PTS,max}$ and $f^{PTS,0}$, standing for the maximum fraction and the minimum fraction that twins could occupy, while f^{PTS} is the current fraction of the PTS in that grain. The Hall-Petch-like barrier law activates only in the grains containing twins.

In the hardening law formulation, the total density of dislocations consists of

$$\rho_{tot}^{s} = \rho_{for}^{s} + \rho_{rev}^{s^+} + \rho_{rev}^{s^-}, \tag{12}$$

where $\rho_{rev}^{s^+}$ and $\rho_{rev}^{s^-}$ are the reversible densities of dislocations on the s^+ and s^- and ρ_{for}^{s} is the forward population. Such split of densities introduces directionality in the hardening law and deformation history dependence. The idea of reversible dislocations was originally implemented in a visco-plastic SC model, which neglects the elastic strain development (Kitayama et al., 2013a; Knezevic et al., 2013a; Mahesh et al., 2004; Rauch et al., 2011). The evolution with shearing strain is (Kitayama et al., 2013a; Kocks and Mecking, 1981)

(If $d\gamma^{s^+} > 0$)

$$\frac{\partial \rho_{for}^{s}}{\partial \gamma^{s}} = (1-p)k_1\sqrt{\textstyle\sum_{s'} g^{ss'}\rho_{tot}^{s'}} - k_2(\dot{\varepsilon}, T)\rho_{for}^{s}, \tag{13a}$$

$$\frac{\partial \rho_{rev}^{s^+}}{\partial \gamma^{s}} = pk_1\sqrt{\textstyle\sum_{s'} g^{ss'}\rho_{tot}^{s'}} - k_2(\dot{\varepsilon}, T)\rho_{rev}^{s^+}, \tag{14a}$$

$$\frac{\partial \rho_{rev}^{s^-}}{\partial \gamma^{s}} = -k_1\sqrt{\textstyle\sum_{s'} g^{ss'}\rho_{tot}^{s'}} \left(\frac{\rho_{rev}^{s^-}}{\rho_0^{s}}\right)^{m}, \tag{15a}$$

(If $d\gamma^{s^-} > 0$)

$$\frac{\partial \rho_{for}^{s}}{\partial \gamma^{s}} = (1-p)k_1\sqrt{\textstyle\sum_{s'} g^{ss'}\rho_{tot}^{s'}} - k_2(\dot{\varepsilon}, T)\rho_{for}^{s}, \tag{13b}$$

$$\frac{\partial \rho_{rev}^{s+}}{\partial \gamma^s} = -k_1\sqrt{\sum_{s'} g^{ss'}\rho_{tot}^{s'}}\left(\frac{\rho_{rev}^{s+}}{\rho_0^s}\right)^m, \tag{14b}$$

$$\frac{\partial \rho_{rev}^{s-}}{\partial \gamma^s} = pk_1\sqrt{\sum_{s'} g^{ss'}\rho_{tot}^{s'}} - k_2(\dot{\varepsilon},T)\rho_{rev}^{s-}. \tag{15b}$$

The material in the initial conditions is assumed to contain $\rho_{for}^s(\gamma^s = 0) = \rho_{0,for}^s$, while $\rho_{rev}^{s+}(\gamma^s = 0)$ and $\rho_{rev}^{s-}(\gamma^s = 0)$ are set to zero. The content approximates an annealed material. Plots illustrating the dislocation populations will be provided later.

In the above equations, k_1 is a fitting parameter controlling the rate of generation, while k_2 is a strain rate and temperature sensitive parameter controlling the recovery of stored dislocations (Beyerlein and Tomé, 2008). The parameter p controls reversibility i.e. separates the portion of reversible and forward densities in the total dislocation density. The parameter ranges between 0 to 1. The value of 1 means a large fraction of reversible dislocations in the total density. The large fraction of reversible dislocations is the likely scenario in case of low content of dislocation debris (Khadyko et al., 2016; Kitayama et al., 2013a; Kocks et al., 1991; Teodosiu and Raphanel, 1991). $g^{ss'}$ can provide flexibility to account for interactions but is taken as an identity. m governs the rate of dislocation recombination (Wen et al., 2015b). ρ_0^s is the density of dislocations at the path reversal for the given system s. The parameter k_2 is calculated using (Beyerlein and Tomé, 2008)

$$\frac{k_2^\alpha}{k_1^\alpha} = \frac{\chi b^\alpha}{g^\alpha}\left(1 - \frac{k_B T}{D^\alpha (b^\alpha)^3} ln\left(\frac{\dot{\varepsilon}}{\dot{\varepsilon}_0}\right)\right). \tag{16}$$

In the above equation, k_B is the Boltzmann constant, $\dot{\varepsilon}_0 = 10^7$ s^{-1} is taken as a reference strain rate, g^α is an effective activation energy, and D^α is the drag stress (Risse et al., 2017; Tam et al., 2020, 2021). Finally, the debris evolves using (Beyerlein and Tomé, 2008)

$$\sum_s \frac{\partial \rho_{deb}}{\partial \gamma^s} = \sum_s q^\alpha b^\alpha \sqrt{\rho_{deb}}\, k_2(\dot{\varepsilon},T)\rho_{tot}^s. \tag{17}$$

In the above equation, q^α is a recovery rate fitting parameter. The parameter separates the accumulated debris portion of dislocations from those annihilated.

4.2 Twinning and de-twinning

Formation of twins influences the microstructure evolution because the twinned domain reorients the crystal lattice orientation relative to the parent grain and the domain introduces a twin-matrix boundary (Beyerlein et al., 2014; Christian and Mahajan, 1995). These changes influence deformation mechanisms and dislocation processes in the microstructure and so the overall flow stress response. The twin-matrix boundaries can hinder slip, which is the barrier effect modeled using Eq. 11. The twin lattice reorientation effects are explicitly accounted for. The twinning is modeled as a pseudo-slip process while the shearing does not involve lattice reorientation (Chin and Mamme, 1969). Once the shearing accumulates to a threshold of 0.01, the pseudo-slip is followed by the reorientation via either the predominant twin reorientation (PTR) method (Van Houtte, 1978) or the volume fraction transfer (VFT) method (Tomé et al., 1991) or the Lagrangian method (Kalidindi, 1998) or the composite grain (CG) method (Proust et al., 2007). The approach to twining in EPSC is the CG method but extended from the original work to consider multiple twin variants in grains. In the CG model, the twin is considered as a separate ellipsoid, and volume is moved from the parent to the twin with pseudo-slip.

In order to circumvent that every twin variant in grains correspond to the one with the highest Schmid factor, twin variant nucleation in the model is influenced by fluctuations in stress concentration following the work presented in (Niezgoda et al., 2014). A fluctuating stress tensor, $\boldsymbol{\sigma}^{c,fluct}$, is added to the criterion for activation per twin system t

$$\mathbf{m}^t \cdot \boldsymbol{\sigma}^c + \boldsymbol{\sigma}^{c,fluct} = \tau^t. \quad (18)$$

Components of $\boldsymbol{\sigma}^{c,fluct}$ are sampled from a multivariable normal probability distribution model using a zero mean, $\sigma_{f,mean}$, and a standard deviation defined as a function of the equivalent stress, σ_{eq}, scaled by the standard deviation parameter $\sigma_{eq}/\sigma_{f,SD}$ for normal and $\sigma_{eq}/(2.5\sigma_{f,SD})$ for shear stress components. The fluctuations have no effect after a twin variant is tagged to nucleate. Subsequent growth of the twinned domain is governed by the hardening law with also no contribution from fluctuations. The stress in the initially formed twinned domain is set according to the finite initial fraction (FIF) scheme (Clausen et al., 2008). The FIF scheme sets the stress to the difference between a stress calculated using the elastic deformation corresponding to the plastic shear caused by twin formation and the stress in the parent grain.

The volume fraction increment for a twinning system evolves using

$$\Delta f^t = \frac{\Delta\gamma^t}{S}, \quad (19)$$

where Δf^t is the increment, while $\Delta\gamma^t$ is the shearing and S is the intrinsic twinning shear, which is 0.189 for Be (Yoo, 1981). The resistance to twin for a variant t, in a mode β is

$$\tau_c^t = \tau_0^\beta + \tau_{HP}^t + \tau_{slip}^\beta, \quad (20)$$

where, τ_0^β is the mode initial twin resistance, τ_{HP}^t is the system barrier term, and τ_{slip}^β is the hardening term due to interaction with dislocations. The barrier term for twinning is defined the same way as for slip. The hardening term is

$$\tau_{slip}^\beta = \mu^\beta \sum_s C^{\alpha\beta}(\dot{\varepsilon}) b^\beta b^\alpha \rho_{tot}^s, \quad (21)$$

where $C^{\alpha\beta}(\dot{\varepsilon})$ is the fitting slip/twin interaction matrix.

Upon cross-reloading, de-twinning can take place. In our approach, de-twinning of a given twin variant in the parent ellipsoid occurs by the activation of the same twin variant inside the twinned domain. Therefore, instead of forming a secondary twinned domain, the volume of the twinned domain that should be occupied by this secondary twin is transferred from the twinned domain back to the parent. However, de-twinning inside the primary twin is allowed to activate in both positive and negative shearing directions as in (Wang et al., 2012). The de-twinning resistance is reset and the hardening of de-twin is modeled the same way as for primary twin using the established parameters. This implies that the Hall-Petch-like term has the opposing effect on the hardening during de-twinning from that during twinning. The parent grain softens, while the twin hardens with the volume evolution during de-twinning. The only difference pertains to the calculation of the mean-free-path inside twins: $d_{mfp}^{s} = \frac{f^{pts} d_c}{\sin(\lambda)}$.

4.3 Backstress law

Backstress in polycrystalline metals governs primarily the unloading and BE characteristics of deformation behavior during cyclic plasticity. Interactions between grains of different crystallography and incompatibilities between hard and soft regions inside grains give rise to backstress (Kassner et al., 2013; Mughrabi, 1983). Backstress acts in the direction opposite to the applied stress during loading (Withers and Bhadeshia, 2001). However, the backstress and applied stresses combine quickly when the loading direction is reversed. Drop in the yield stress upon reversal is a signature of backstress. The role of backstress on the flow stress change in cross-reloading or any other strain-path-change other than reverse loading is smaller. The EPSC model is formulated to account for the elastic interactions between individual grains and HEM. A phenomenological law to account for backstress inside grains in EPSC is summarized next.

The law captures kinematic hardening effects per slip system (Feng et al., 2020; Harder, 1999; Zecevic and Knezevic, 2015)

$$\tau_{bs}^{s} = \mathbf{m}^{s} \cdot \boldsymbol{\sigma}_{bs}^{c} = 2 \sum_{s'} \mathbf{m}^{s} \cdot \mathbf{m}^{s'} \tau_{bs,sys*}^{s'} , \tag{22}$$

where

$$\tau_{bs,sys*}^{s'} = \begin{cases} \tau_{bs,sys}^{s'} \text{ if } \tau_{bs,sys}^{s'} > 0 \\ 0 \text{ if } \tau_{bs,sys}^{s'} < 0 \end{cases} . \tag{23}$$

In these equations, $\boldsymbol{\sigma}_{bs}^{c}$ is the grain-level backstress tensor formed by summing over the slip system backstress sources. The slip system backstress is

(if $d\gamma^{s^{+}} > 0$ and $\tau_{bs,sys}^{s^{+}} > 0$)

$$\tau_{bs,sys}^{s^{+}} = \tau_{bs}^{sat}\left(1 - \exp\left(-\nu\gamma^{s^{+}}\right)\right), \tag{24}$$

$$\tau_{bs,sys}^{s^{-}} = -A\tau_{bs,sys}^{s^{+}}, \tag{25}$$

(if $d\gamma^{s^{+}} > 0$ and $\tau_{bs,sys}^{s^{+}} < 0$)

$$\tau_{bs,sys}^{s^{+}} = -(A+1)\tau_{bs}^{sat} \exp\left(-\frac{\gamma^{s^{-}}}{\gamma_b}\right) + \tau_{bs}^{sat}, \tag{26}$$

$$\tau_{bs,sys}^{s^{-}} = -\frac{1}{A}\tau_{bs,sys}^{s^{+}}. \tag{27}$$

Calibration parameters pertaining to the above phenomenological law include a saturation term, τ_{bs}^{sat}, a constant A to enable an asymmetric evolution of backstress in directions $s+$ and s-, additional fitting constants γ_b and ν, and γ^s is the shearing strain at the point of strain-path-change. Note that the backstress matrix, $h_{bs}^{ss'}$, is derived from these equations. Note that $\tau_{bs}^{s^+}$ opposes the driving force in s^+: $\mathbf{m}^{c,s+} \cdot \boldsymbol{\sigma}^c - \tau_{bs}^{c,s+} = \tau_c^{c,s}$, which means that τ_{bs}^{c,s^+} reduces the driving force. In contrast, τ_{bs}^{c,s^-} aids the driving force in s^-: $\mathbf{m}^{c,s-} \cdot \boldsymbol{\sigma}^c - \tau_{bs}^{c,s-} = \tau_c^{c,s}$. Plots illustrating the effects will be provided shortly.

The above phenomenological description of slip system-level kinematic hardening effects have proven suitable to capture the phenomena governing nonlinear unloading and the BE in cyclic loading of steels (Zecevic et al., 2016b), Al alloys (Barrett and Knezevic, 2019), and orthorhombic uranium (Barrett et al., 2020). In think work, we use the law to model loading and cross-reloading of Be.

5. Results

Figure 4 shows pole figures of the initial texture in the Be plate. The texture is relatively sharp with **c**-axis predominantly aligned with the TT direction and slightly tilted towards IP1. The measured texture is represented using 500 weighted orientations for modeling using the texture compaction procedure described in (Barrett et al., 2019; Eghtesad et al., 2018b; Knezevic and Landry, 2015). Pole figures based on the 500 weighted orientations used in the simulations are indistinguishable from the pole figures showing the measured data and are not shown. Given the texture, grains are favorably oriented for twinning and prismatic slip in compression along IP1, while for pyramidal slip in compression along TT. Nevertheless, basal slip is likely to operate in both of these loading scenarios because it is the softest deformation model in Be. The initial grain size in the material is 25 μm (Brown et al., 2012).

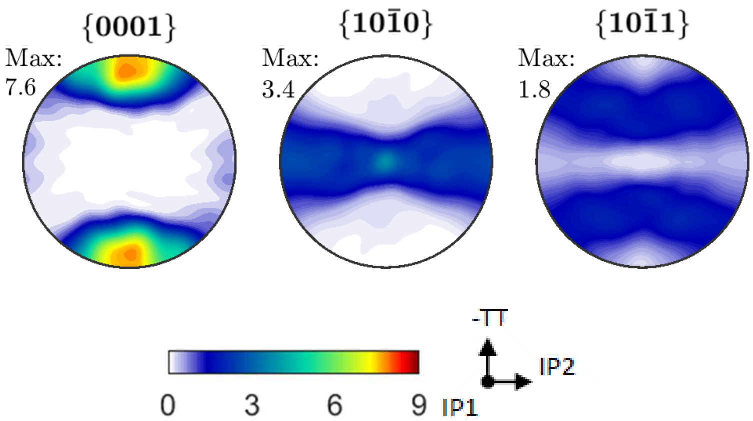

Figure 4: Pole figures showing the initial texture in the rolled plate of Be.

Plastic deformation of Be at room temperature is carried out by basal slip $\{0002\}\langle 11\bar{2}0\rangle$ as the easiest to activate slip systems, by prismatic slip $\{10\bar{1}0\}\langle \bar{1}2\bar{1}0\rangle$ requiring a higher activation stresses, and by pyramidal 1st order $\{10\bar{1}1\}\langle \bar{1}\bar{1}23\rangle$ and 2nd order $\{2\bar{1}\bar{1}2\}\langle 2\bar{1}\bar{1}3\rangle$ slip systems, which are the most difficult to activate (Aldinger, 1979; Jonsson and Beuers, 1987; Poirier et al., 1967). The material can also deform by extension twinning, $\{10\bar{1}2\}\langle \bar{1}011\rangle$, the most common twin in HCP metals (Beyerlein et al., 2014; Christian and Mahajan, 1995; Partiridge, 1967). These twins re-reorient the basal pole for 84.4° from perpendicular to parallel with the compression direction. As a result of such texture changes, fraction of twinning can be estimated from texture measurements (Brown et al., 2012; Feather et al., 2019). These four deformation modes are made available per grain in the MS-EPSC model for modeling plastic deformation of Be.

The simulations began with a cooling step to estimate the initial stress state in the grains using a crystal thermal dilatation tensor for Be consisting of α_{11} = 12.42x10^{-6} K^{-1}, α_{22} = 12.42x10^{-6} K^{-1}, α_{33} = 9.881x10^{-6} K^{-1}. The dilatation tensor components are used to estimate the initial state of thermal inter-granular residual stresses using Hooke's law at the crystal-level $\dot{\boldsymbol{\sigma}}^c = \mathbf{C}^c\left(\dot{\boldsymbol{\varepsilon}}^c - \boldsymbol{\alpha}^c\dot{T}\right)$, assuming a uniform temperature rate over the polycrystal of $\dot{T}$ = 80 K per increment in time. Note that $\mathbf{C}^c$ and $\boldsymbol{\alpha}^c$ are dependent on crystal orientation of grain c, in addition to crystal constants. An equivalent linear relation at the polycrystal level is $\dot{\boldsymbol{\sigma}} = \mathbf{C}\left(\dot{\boldsymbol{\varepsilon}} - \boldsymbol{\alpha}\dot{T}\right)$. The cooling is performed from 850 K processing temperature to 300 K. The subsequent strain-path-change deformation sequence is performed after only adjusting the boundary conditions to simple compression with none of the microstructural variables or residual stress reset. The compression boundary conditions are uniaxial along the loading direction along with the traction-free surfaces in the orthogonal directions. The loading direction was adjusted for the cross-reloading boundary conditions, while preserving the microstructure, state variables, and residual stress field.

Figure 5 compares measured and simulated true-stress-true strain response for the fourteen loading and cross-reloading scenarios (Table 1). To calibrate the model parameters, B, E, J, K, and N loading sequences were used. These loading sequences sufficiently covered the range of imposed loading directions, pre-strain levels, and strain rates to establish the parameters. For example, the loading conditions in B are like those in A. One is sufficient for fitting, while the other can be used for verification. Likewise, the loading conditions in E are similar to those in D and F. Adding more loading sequences to the parameter identification procedure did not change the parameters appreciably i.e. did not influence the quality of fits. The remaining tests are not part of the fitting procedure but predictions. Overall, the achieved agreement for all tests is good. The high strain rate stress-strain curves are slightly overpredicted, which is attributed in part to not modeling softening due to adiabatic heating. As can be seen, some experimental results are missing in the figure. The specimens in A, G, and H were successfully deformed to the given strain levels under the given strain rates but load was not recorded. The predictive accuracies for the stress-strain curves in A, D, and F are not as good as for the other conditions. The loading sequences in A, B, and C are different only in the pre-strain level. However, the experimental stress-strain curve upon reloading in A is more compliant than those in B and C. Therefore, the poor prediction in the A sequence is attributed to the experimental setup recording a more compliant curve than the real material behavior as in B and C. Poor predictions in the loading sequences D and F are due to the texture evolution, which is governed by the rate of de-twinning. The predicted rate for these conditions is slower than in the experimental measurements, as will be elaborated shortly.

Table 2 presents the model parameters established for Be. The parameters identified for Be are the initial resistance to slip, τ_0^α, trapping rate coefficient, k_1^α, drag stress, D^α and activation barrier for de-pinning, g^α, per slip mode and the initial resistance to twin, τ_0^β, interaction matrix, $C^{\alpha\beta}$, and Hall-Petch parameter HP^β per twinning mode. The identification procedure started by varying τ_0^α and τ_0^β to reproduce onset in yielding. Next, k_1^α, was varied such that the initial hardening slopes are captured. Next, g^α , D^α, HP^β, and $C^{\alpha\beta}$ are varied to match the latter hardening rates. Finally, q^α was fit to capture the later stage in the hardening rates. Concurrently with the hardening parameters, the backstress law parameters were identified. These included the saturation value for backstress τ_{bs}^{sat}, asymmetry factor, A, and coefficients ν and γ_b. τ_{bs}^{sat} and A were varied to improve the yield after strain-path change. Once these were achieved, tuning ν and γ_b simply provides better fits. The table also presents the Burgers vectors and the initial dislocation density. Additionally, the crystal elastic constants for Be are: C_{11} = 292.3 GPa, C_{12} = 26.7 GPa, C_{13} = 14.0 GPa, C_{33} = 336.4 GPa, and C_{44} = 162.5 GPa (Kocks et al., 1998). Based on these crystal constants, shear modulus for prismatic slip is 132.8 GPa, for basal slip is 162.5 GPa, for pyramidal slip is 152.3 GPa and for extension twinning is 150.3 GPa.

Figure 6 shows basal pole figures depicting the measured and simulated texture evolution after preloading and cross-reloading compression tests. The basal pole intensity forms along the initial IP1 compression direction as a signature of deformation twinning activity. Upon cross-reloading in the TT direction the initial twins along IP1 are depleted due to de-twinning. However, basal pole density forms upon cross-reloading in the IP2 direction due to twinning, while the formed intensity is slightly depleting due to de-twinning. As is evident, the calculated texture evolution achieves excellent agreement. Comparison of the pole figures is inherently qualitative. To make a quantitative comparison between the experiment and simulation, Figure 7 shows the evolution of the twin volume fraction after pre-loading and after cross-reloading for ten *in-situ* tests. Strong strain rate dependence of the twin volume fraction can be inferred. More detailed evolution of twin volume fraction is measured and simulated for the sample K. Overall, the model can be regarded as capable of capturing the evolution of twin volume fractions. However, the predictive accuracies vary amongst the loading sequences. While the model successfully predicts a substantial amount of extension twinning activity after the pre-compression along IP1 under 2000/s strain rate, the predictive accuracies of the twin volume fractions after cross-reloading for the D, E, and F cases are worse than the other cases. These cross-reloading deformation cases along the TT direction are characterized by substantial de-twinning. The model favors rather slip over de-twinning. The relative activities of deformation modes are direct consequences of underlying resistances. If resistances to slip were predicted higher than achieved in the model, then de-twinning would be easier. Given that we established a set of model parameters providing the best compromise in predicting all the data, improvements of the model such as accounting for spreads in the field variables over ellipsoids are necessary to improve these predictions. In the present model, a single value is assumed for a given field across the entire ellipsoid. Such spreads have been incorporated in a visco-plastic SC (VPSC) formulation and the predictive characteristics have improved (Lebensohn et al., 2016; Zecevic et al., 2020; Zecevic et al., 2018, 2019a; Zecevic et al., 2017).

Finally, Fig. 8 shows measured and predicted evolution of elastic lattice strains for the ten *in-situ* tests. Lattice strains calculated from diffracting planes with poles parallel and perpendicular to loading are distinguished as are those from sample loading and unloading. Accuracy of the calculated lattice strains is a function of the peak-fitting accuracy in GSAS-II. When diffraction peaks have low intensity there are few diffracting volumes being measured and peak position can be difficult to determine. The error associated with peak position propagates through to the lattice strains calculated for a given diffracting plane. It also should be noted that peak-fitting accuracy evolves with strain i.e. with texture changes. For example, de-twinning causes the basal poles originally oriented along the IP1 to reorient along the TT; therefore, because $\{0002\}$ diffracting volumes increase in number with cross-reloading compression in TT, $\{0002\}$ peaks are easier to fit for the diffracting planes with poles along TT after cross-loading. Nevertheless, the lattice strains evolve relatively linearly in the loading direction, while very little in the perpendicular direction. This is a unique feature of Be because of nearly zero Poisson's ratio. Although certain nonlinearities appearing during unloading in most of the experimental results are not present in the simulation results, we regard these predictions as good. In particular, the magnitude in stress versus strain and trends in the loading direction versus the perpendicular direction are captured by the model. These predictions signify that that the residual stress fields should be predicted accurately.

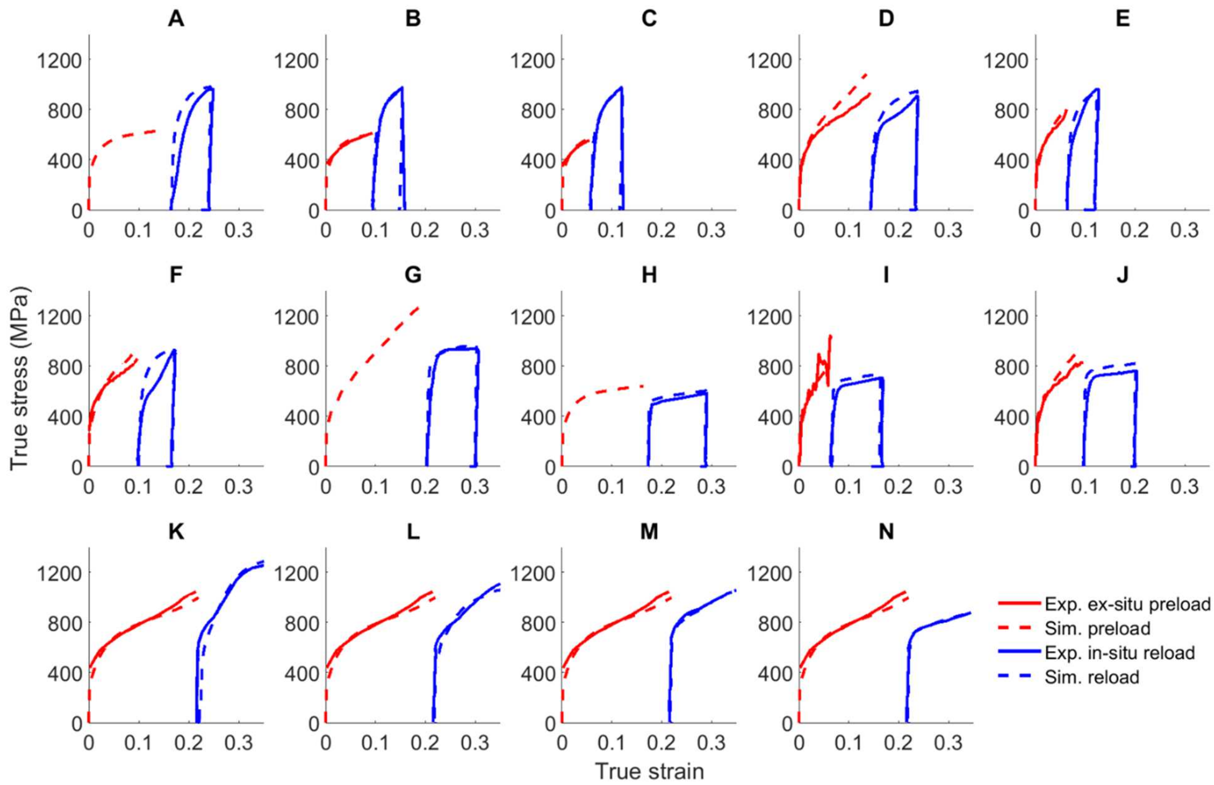

Figure 5: Measured (Exp.) and simulated (Sim.) true stress-true strain response of Be during *ex-situ* pre-loading and *in-situ* reloading. Although compressive, the stress and strain are plotted as positive.

Table 2: Model parameters for the evolution of slip system and twin system resistances in Be. Self-interaction ($L^{\alpha\alpha}$) and planar interaction latent hardening ($L^{\alpha\alpha'}$) constants are set to 0.15, while the rest of the latent hardening interactions are small and therefore set to zero according to (Bertin et al., 2014).

Slip systems	$\alpha = 1$ Prismatic	$\alpha = 2$ Basal	$\alpha = 3$ Pyramidal
b^{α} $[m]$	2.28×10^{-10}	2.28×10^{-10}	4.24×10^{-10}
g^{α}	9.75×10^{-3}	5.75×10^{-3}	4.5×10^{-3}
k_1^{α} $[m^{-1}]$	2.5×10^{8}	0.15×10^{8}	1.6×10^{9}
D^{α} $[MPa]$	600	450	650
$\rho_{0,for}^{\alpha}$	1.5×10^{12}	1.5×10^{12}	1.5×10^{12}
τ_0^{α} $[MPa]$	110	25	233

HP^{α}	0.05			0.02			0.02	
q^{α}	5			6			0	
Twin system						$C^{\alpha\beta}$		
	b^{β} $[m]$	f_0^{PTS}	f_{max}^{PTS}	τ_0^{β} $[MPa]$	HP^{β}	$\alpha = 1$	$\alpha = 2$	$\alpha = 3$
$\beta = 1$	2.64×10^{-11}	0.05	0.95	331	0.2	$3500 - 100ln\frac{\dot{\varepsilon}}{1s^{-1}}$	$1100 - 100ln\frac{\dot{\varepsilon}}{1s^{-1}}$	$1400 - 100ln\frac{\dot{\varepsilon}}{1s^{-1}}$
De-twin				30	0.2	30	30	30
Backstress parameters	τ_{bs}^{sat} $[MPa]$		v		γ_b		A	
	20		1		0.001		10	
Fluctuating stress	$\sigma_{f,mean}$		$\sigma_{f,SD}$		Reversible dislocations constants		p	m
	0		10				1.0	0.5

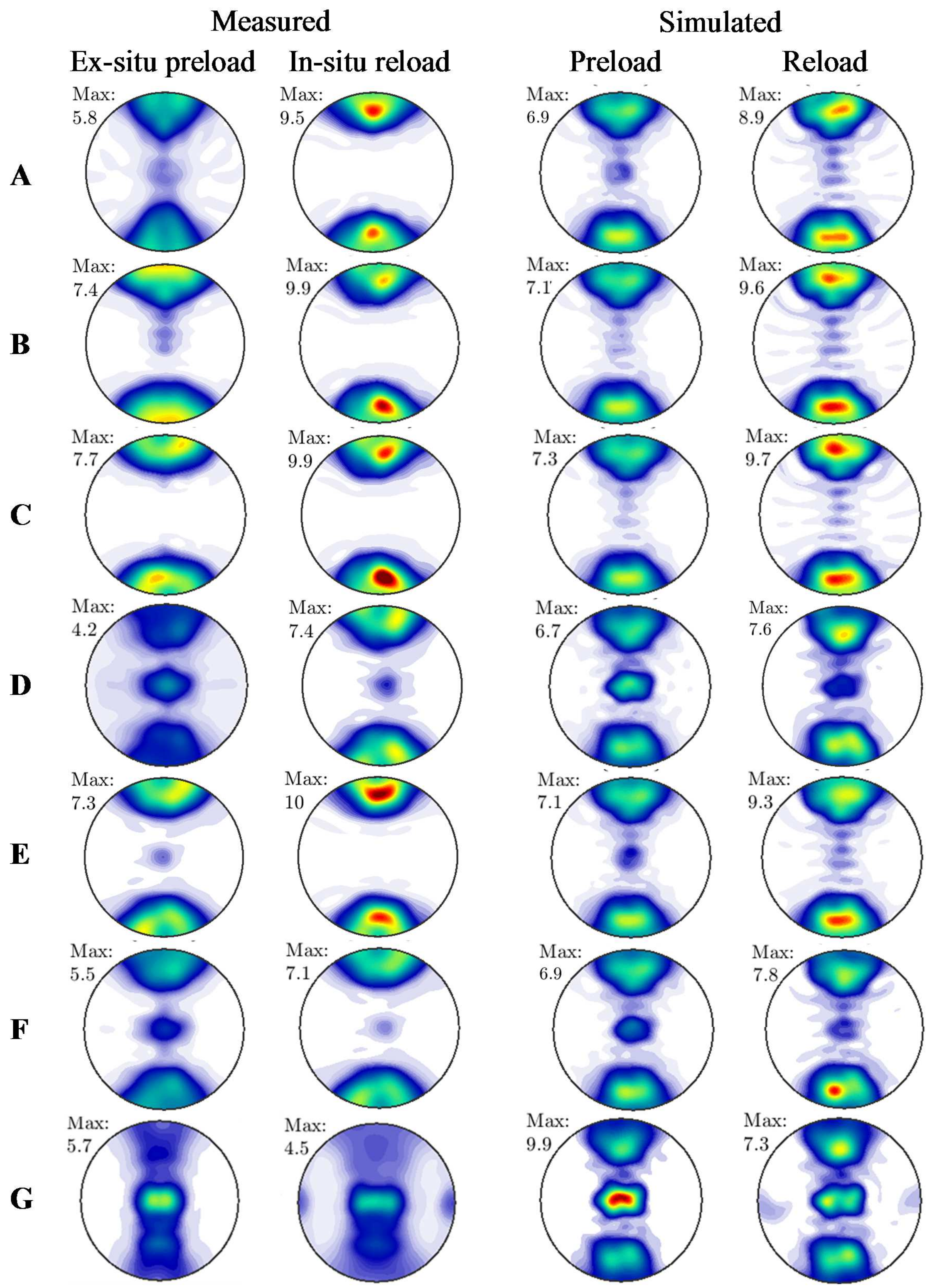
Measured
Simulated
Ex-situ preload
In-situ reload
Preload
Reload
A
B
C
D
E
F
G
Max: 5.8
Max: 9.5
Max: 6.9
Max: 8.9
Max: 7.4
Max: 9.9
Max: 7.1
Max: 9.6
Max: 7.7
Max: 9.9
Max: 7.3
Max: 9.7
Max: 4.2
Max: 7.4
Max: 6.7
Max: 7.6
Max: 7.3
Max: 10
Max: 7.1
Max: 9.3
Max: 5.5
Max: 7.1
Max: 6.9
Max: 7.8
Max: 5.7
Max: 4.5
Max: 9.9
Max: 7.3

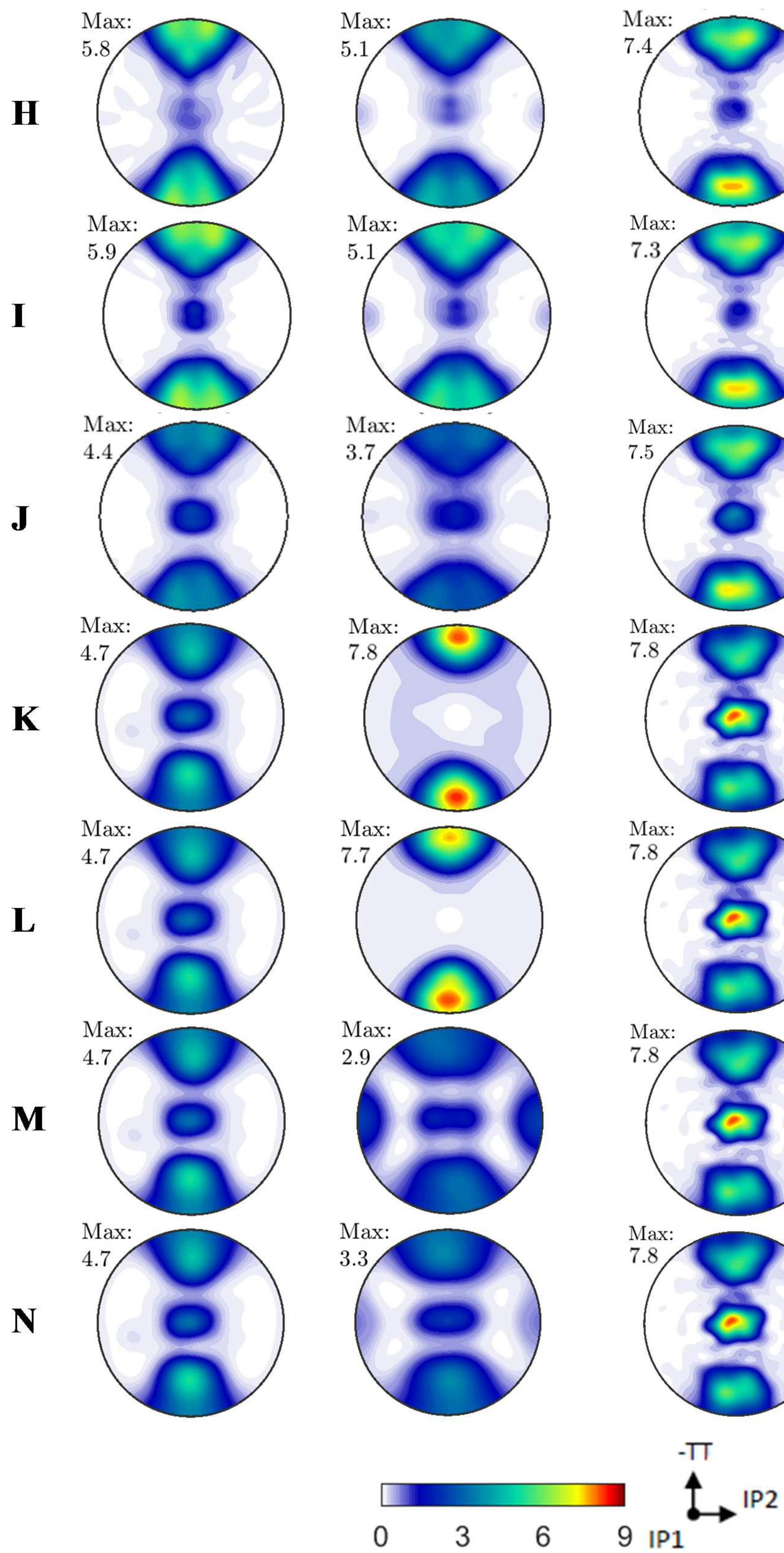

Figure 6: {0001} pole figures showing the crystallographic texture evolution in the samples of Be after preloading and after reloading. Pole figures were calculated from ODFs that were

generated in Maud using the E-WIMV texture algorithm when performing a full texture analysis on the 576 histograms created by integrating the 2D X-ray diffraction patterns collected for each sample at each of the 8 rotation angles. Pole density is plotted in units of multiple of a random distribution (m.r.d.).

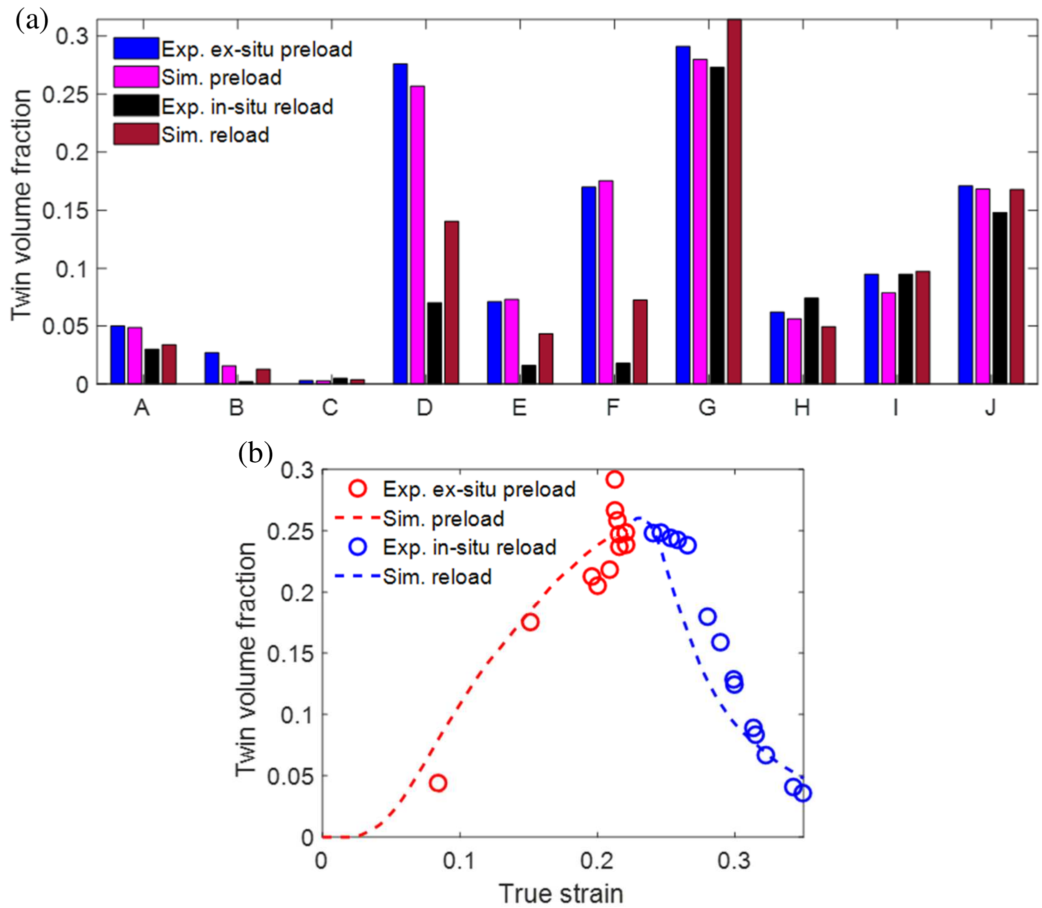

Figure 7: (a) Comparison of measured and predicted twin volume fraction in the A-J samples of Be after preloading and after reloading. (b) Comparison of measured and predicted evolution of the twin volume fraction during the deformation of the sample K. The measurements during the reload in (b) are based on *in-situ* integrated {0002} peak intensities taken from (Brown et al., 2013).

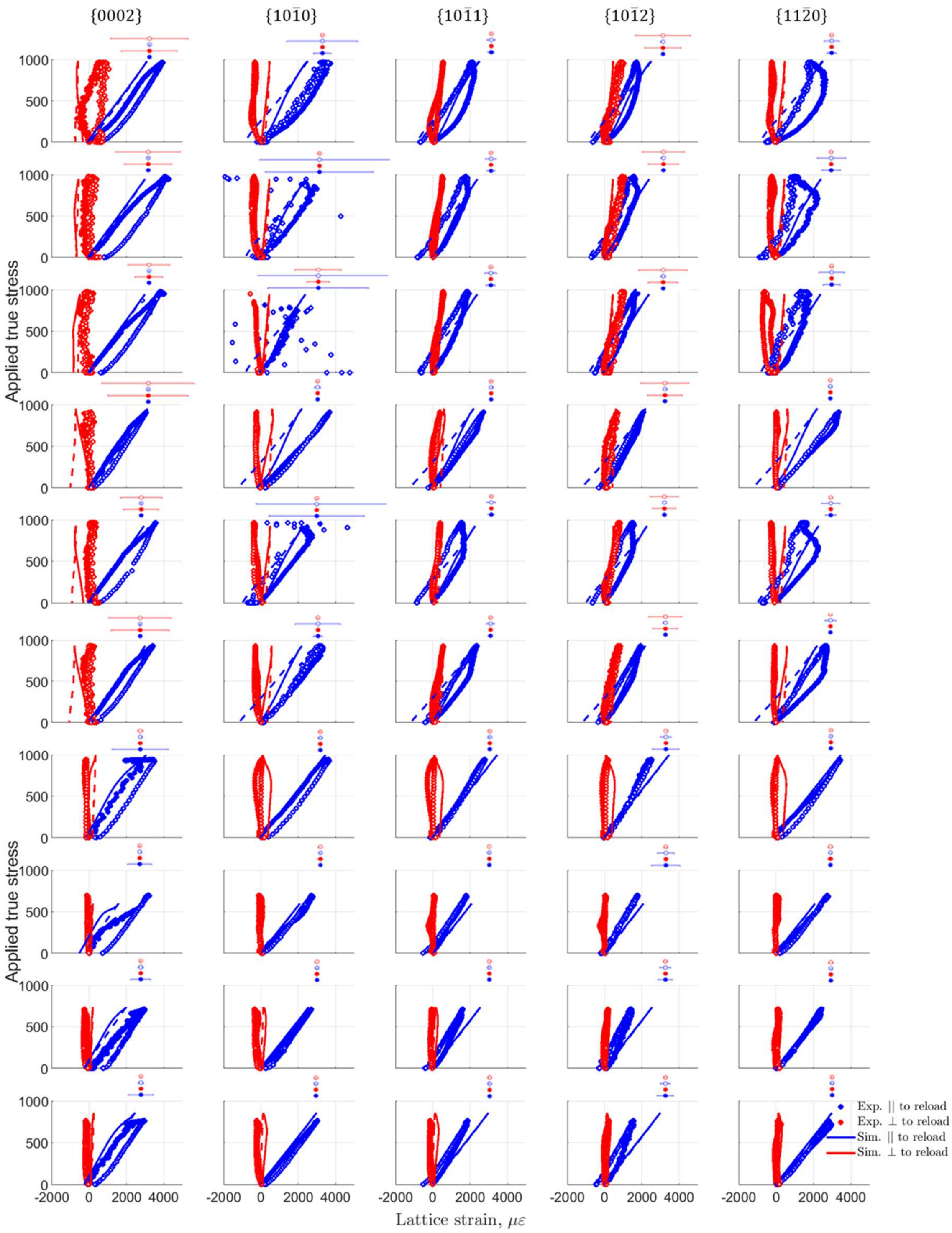

Figure 8: Measured and predicted evolution of lattice strains for several diffracting planes in the A-J samples with poles parallel (blue) and perpendicular (red) to the loading direction. Solid circles are the experimental loading path, while the hollow circles are the experimental unloading path. Solid lines are simulated loading, while the dash lines are simulated unloading. These hkl-

specific lattice strains were measured via X-ray diffraction during *in-situ* compressive loading and unloading. Sign of stress and lattice strain is changed from negative to positive. The error bars indicate the average uncertainty in each experimentally-determined lattice strain dataset.

6. Discussion

This work has advanced a formulation of the EPSC crystal plasticity modeling framework termed the MS-EPSC model to interpret the deformation behavior of Be. The studied material deforms by multiple slip modes having different resistances to activation and deformation twinning, thereby providing a challenging test for the model, especially to predict the strain-path sensitive deformation. The strain paths consisted of compressive loading in one direction and then compressive cross-loading in another direction while varying strain levels and strain rates. The loading tests were performed *ex-situ*, while the reloading tests were carried out *in-situ* under the high energy synchrotron X-ray diffraction. Procedures are developed to obtain texture, twinning, and elastic lattice strains from the diffraction data.

The material shows significant strain rate sensitivity from 0.001/s to 5/s to 2000/s during the IP1 compression. The curves at high strain rate exhibit a sigmoidal hardening shape due to profuse twinning. Likewise, the cross-reloading is strain rate sensitive from 0.0002/s to 0.001/s to 5/s. The strain rate dependence is attributed to slip mechanisms becoming increasingly more difficult to activate at higher strain rates, which is embedded in the thermally activate hardening law. Therefore, the increase in the flow stress at a given strain under high strain rate increases the activity of deformation twinning. The flow stress at the end of the pre-compressed material at 0.001/s is lower than the flow stress of the subsequent cross-reloading in the TT direction at 0.0002/s. Moreover, a substantial increase in the hardening rate arises upon the change from the IP1 compression to the cross-compression in the TT direction. However, the flow stress at the end of the pre-compressed material at 5/s and 2000/s is higher than the flow stress of the subsequent cross-reloading in the TT direction or the IP2 direction. The drop in the stress is followed by an increase in the hardening rate upon the change from the high strain rate IP1 compression to the quasi-static cross-compression in the TT direction. A small transient in flow stress and a low hardening rate characterize the strain-path-change change from IP1 compression to IP2 compression, unless the IP1 compression was under high strain rate, which would cause a drop in the flow stress. It is shown that the model is able to capture these particularities pertaining to the complex strain-path-change and strain rate sensitive deformation of the material including the evolution of texture, twinning, lattice strains, flow stress, and anisotropic hardening with great accuracy using a unique set of single-crystal hardening parameters.

Figure 9 shows the predicted slip/twin activities associated with the predicted flow curves. The predictions are the average slip/twin activity considering all parent grains and twinned domains. The results reveal that prismatic and basal slip predominantly carry out the compressive deformation in the IP direction. The plots show a substantial extension twinning activity under 5/s and 2000/s strain rate pre-compression. Some pyramidal slip arising and a slight increase in the basal slip activity are due to the deformation of extension twinning domains. Comparatively, pre-compression at the lower rate 0.001/s shows much less extension twinning as shown in the evolution of texture and twin volume fractions. The cross-reloading deformation in the TT direction is characterized by basal and pyramidal slip and substantial de-twinning. Since de-twinning does not involve nucleation prior to growth like in twinning but simply reversing of the interface direction, resistance to de-twinning is smaller than that of twinning (Partridge and Roberts, 1964). As cross-reloading in the TT proceeds, the intensity of the basal planes formed along the IP1 direction is depleting and the twin volume fraction decreases. Cross-reloading in the IP2 direction is carried out by prismatic and basal slip and some twinning and de-twinning. A new intensity in the basal poles arises along the IP2 direction. As the cross-reloading in the IP2 changes the stress state in the grains with respect to the loading direction, the twins forming upon the IP2 cross-reloading are different variants from those formed in the IP1 loading path. The measured volume fraction of twins after the secondary deformation step show similar content meaning that there is a balance of some twinning and some de-twinning. In summary, existing variants are decreasing in their volume fraction for the TT cross-reloading, while new twin variants are increasing in their volume fraction for the IP2 cross-reloading.

Primarily due to the shifts in active deformation mechanisms, the MS-EPSC model captures the transients in the flow stress upon strain-path-changes. The mechanisms carrying the plasticity are different per path. The model successfully predicts the flow stress starting from the initial state of the primary loading to the end of the cross-reloading path for all tests. Therefore, the hardening behavior is predicted, in addition to the shifts in active deformation mechanisms governing the transient. The predictions of hardening during the strain-path-changes is primarily attributed to the flow of polarized or reversible dislocations (Kitayama et al., 2013b; Knezevic et al., 2013a; Peeters et al., 2001; Rauch et al., 2011) as well as twinning/de-twinning. The model formulation facilitate that a portion of the previously generated reversible dislocations annihilate during a reload to predict the hardening behavior. Annihilation of dislocations at a strain-path-change were confirmed by looking into the reductions of diffraction peak widths (Wilson and Bate, 1986). Therefore, a decrease in dislocation density at strain-path-change is a phenomena that should be considered by the model to enable predicting hardening during strain-path-changes.

The effect of reversible dislocation populations for the reversibility parameter of unity is shown in Fig. 10a. The figure shows a typical evolution of the dislocation densities with accumulated shear strain on a slip system. The easy motion and annihilation of loosely tangled dislocations in the opposite direction is facilitated by the high value of the reversibility parameter. As a result, the formulation mediates the issue of over-predicting of the hardening upon the strain-path-change. Figure 10b shows that the increasing trend in the total dislocation density is a strong function of strain rate. Note that the hardening law formulation is strain rate and temperature sensitive. In the figure, only the total dislocation density governing hardening is meaningful because $s+$ and $s-$ are not selected with respect to the loading direction but randomly. Therefore, only the total dislocation density is provided. The drop in flow stress arises regardless of the TT or IP2 strain-path-change after the high strain rate IP1 compression, which means that the glide of reversible dislocations is dependent on the cross-reloading pathway. Upon the initial changes in the dislocation density, subsequent dislocation generation is much more rapid in the TT direction along with de-twinning than in the IP2 direction along with twinning and de-twinning.

Good predictions of the strain-path-change deformation behavior of Be results from a combination of several distinct physical phenomena incorporated in the model. The evolution of slip system-level backstress and inter-granular backstress are the remaining phenomena the model accounts for. Figure 11 shows a typical buildup of intra-granular backstress on a slip system with shearing. The calibrated backstress law is approximate because the accurate calibration of the law requires load reversal or cyclic data, which are currently not available for Be. Therefore, the effect is regarded as secondary. The inter-granular sources of backstress fields are the interactions between individual grains of different crystal orientations. These effects are approximated in the EPSC model because every grain interacts with the averaged polycrystalline response unlike in full-field models in which grain-to-grain interaction are explicitly modeled. At zero applied stress, these inter-granular stress fields become residual stress fields. Fig. 12 shows a comparison between simulation results performed with and without residual stress. To obtain the predictions without residual stress, grain stress is set to zero at the zero overall flow stress after the pre-loadings. The inter-granular residual stresses effects after one strain path influencing the subsequent path are determined as small because the magnitude of these stresses is below yield stress of the material. From the comparison of the curves with and without inter-granular stresses, it is evident that the inter-granular stresses are slightly aiding plastic deformation in the subsequent path. Interestingly, the effect is directional being larger in the IP1 cross compressions than in the TT cross compressions.

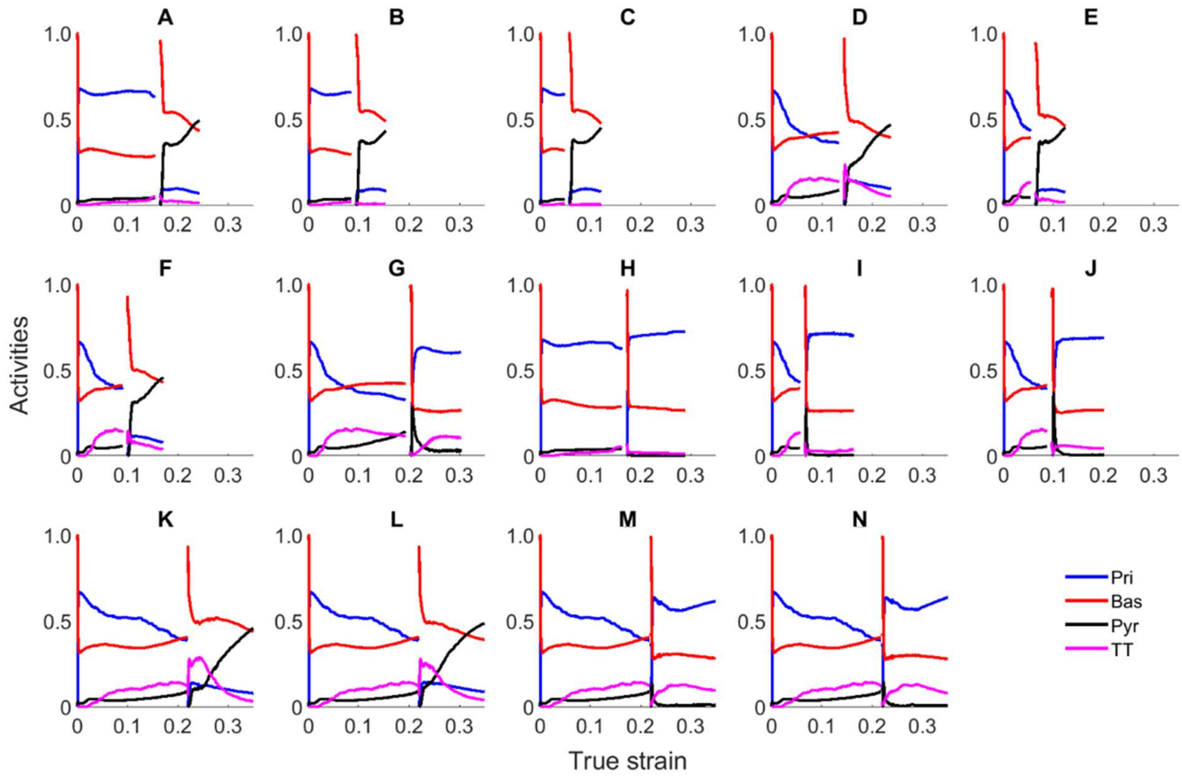

Figure 9: Predicted activities of the prismatic (Pri.), basal (Bas.), pyramidal (Pyr.) and tensile twinning (TT) deformation modes for the selected preload and reload cases.

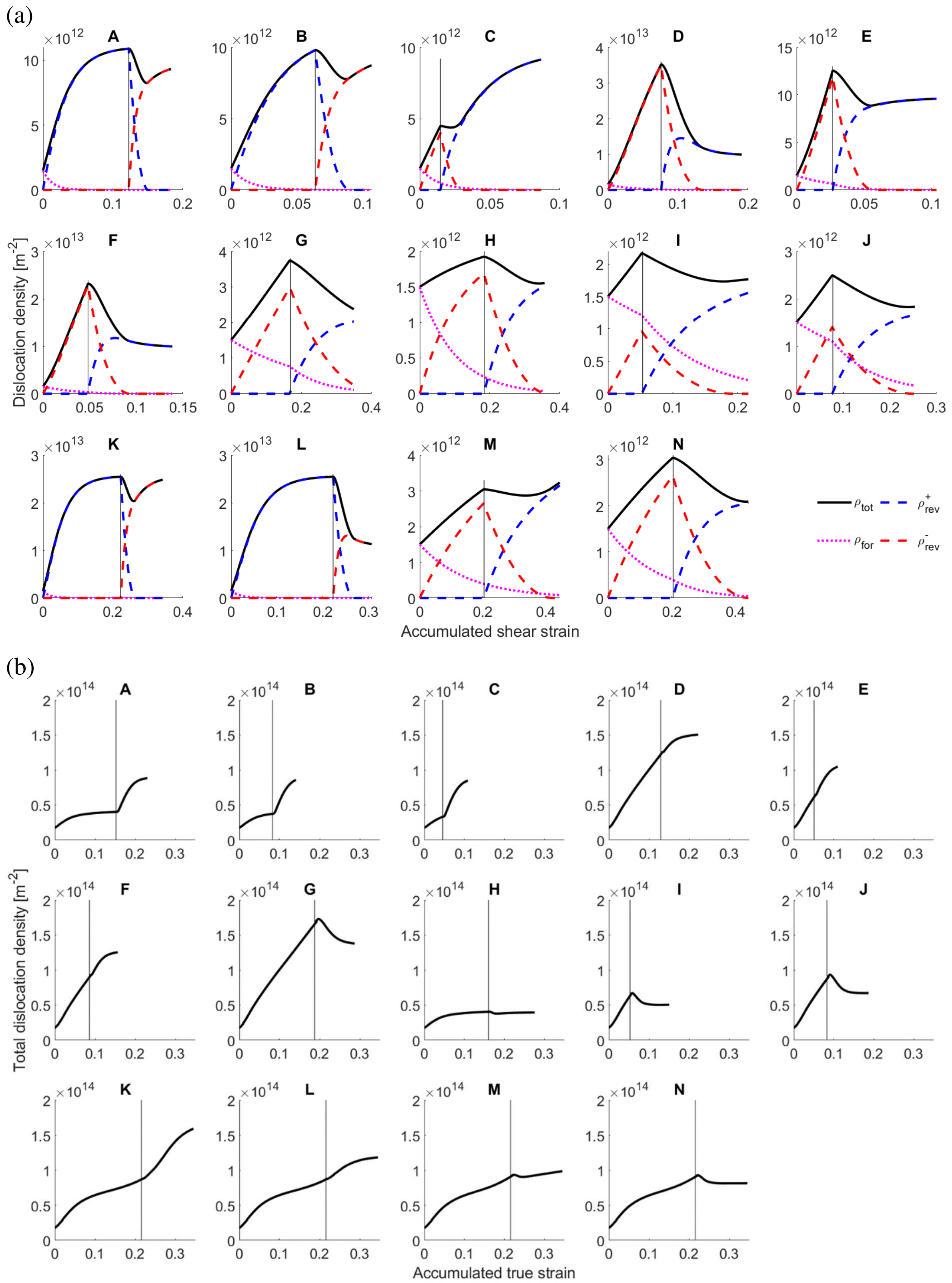
(a)
A
B
C
D
E
F
G
H
I
J
K
L
M
N
Dislocation density [m^-2]
Accumulated shear strain
ρ_tot
ρ⁺_rev
ρ_for
ρ⁻_rev
(b)
Total dislocation density [m^-2]
Accumulated true strain

Figure 10: (a) Simulated evolution of the dislocation density populations with accumulated shear strain in a randomly selected grain for a slip system with the highest activity: $(0\bar{1}10)[2\bar{1}\bar{1}0]$ for A, B, K, and L, $(\bar{1}100)[\bar{1}\bar{1}20]$ for C, D, E, and F, and $(0001)[2\bar{1}\bar{1}0]$ for G, H, I, J, M, and N. (b) Simulated evolution of the total dislocation density with true strain during the loading and reloading. The values are summed over the slip systems in every grain and then averaged over the polycrystal.

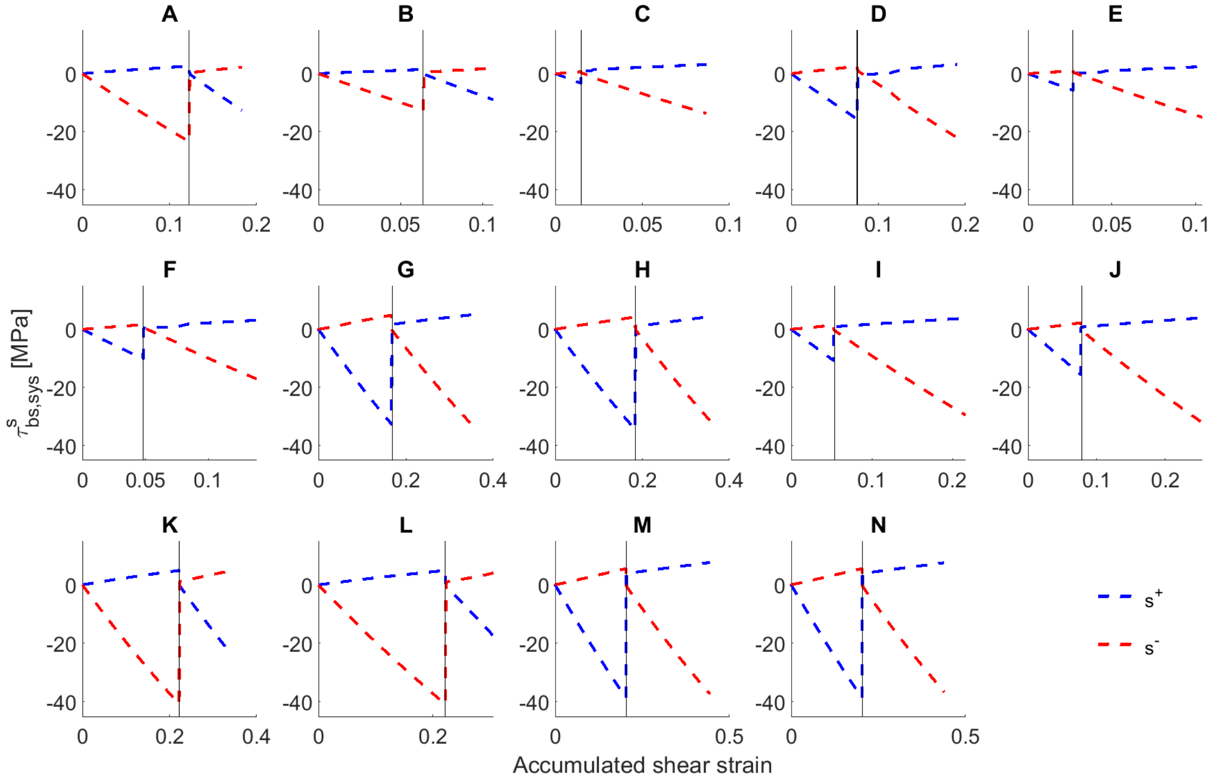

Figure 11: Backstress with accumulated shear strain in the same grain and slip system as in Fig. 10a.

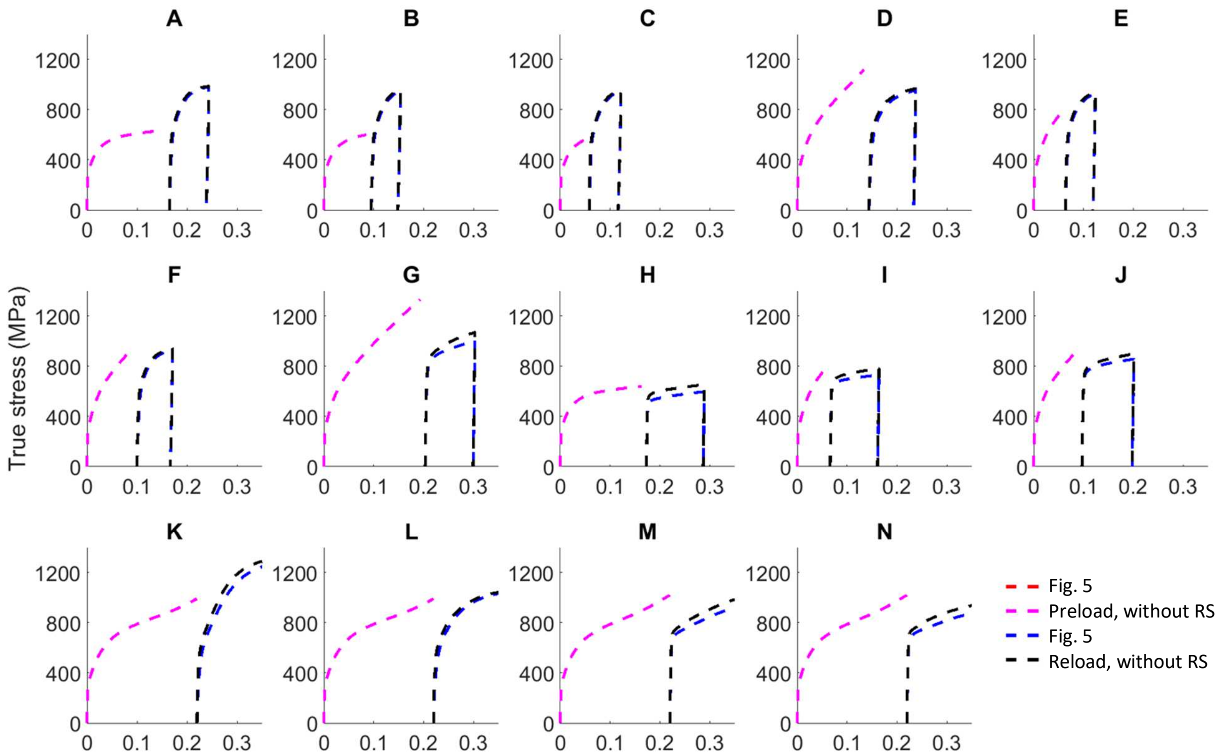

Figure 12: Comparison of true stress-true strain simulation results performed with and without residual stress (RS).

7. Summary and conclusions

In this work, we have described the deformation behavior of pure Be during compressive loading and cross-reloading based on mechanical testing as a function of strain rate, *in-situ* high energy synchrotron X-ray diffraction characterization, and crystal plasticity modeling. Several procedures have been developed to obtain texture, twinning, and elastic lattice strains from the diffraction data. Mechanical response of the material has been measured *ex-situ* and *in-situ* for fourteen strain-path-change tests under several strain rates. The data shows a substantial increase in the initial flow stress and hardening rate upon the change from the IP1 compression to the cross-compression in the TT direction. In contrast, a drop in the stress and increase in hardening rate at the beginning of the second path arises upon the change from the high strain rate IP1 compression to the quasi-static cross-compression in the TT direction. A small transient in flow stress and a low hardening rate characterize the strain-path-change change from IP1 compression to IP2 compression, unless the IP1 compression was under high strain rate, which would cause a drop in the flow stress.

The comprehensive testing and characterization data sets are compared with the predictions of an EPSC crystal plasticity model termed MS-EPSC. The model incorporates several sub-models, namely, an advanced thermally activated dislocation-based hardening law, twin activation via statistical stress fluctuations, reorientation of one or multiple twin domains within a grain and associated stress relaxation, twin barrier hardening, and de-twinning. The studied material deforms by multiple slip modes having different resistances to activation and deformation twinning, thereby providing a challenging test for models, especially to predict the strain-path sensitive deformation. To better capture the strain-path-change deformation of HCP Be, the model is advanced in several aspects. The improvements pertain to the incorporation of dissolution of dislocation population upon the load reversal, slip system level backstresses, and latent hardening. The model is able to capture the particularities pertaining to the complex strain-path-change and strain rate sensitive deformation of the material including the evolution of texture, twinning, lattice strains, flow stress, and anisotropic hardening with great accuracy using a unique set of single-crystal hardening parameters.

While reproducing the data, the model adjusts the relative activity of slip systems for some strain paths and low strain rates, while hard versus soft slip systems and de-twinning or slip, twinning, and de-twinning for other deformation paths. From the comparison of the experimental data and predictions, we infer that these shifts in active deformation mechanisms are primarily responsible for transients in the flow stress from one path to another and hardening. For further verification of these observations, good agreement in predicting the evolution texture and twin fraction is achieved. Additionally, the evolution of elastic lattice strains compare well with the data measured *in-situ* using the high-energy x-ray diffraction. The secondary effects improving the predictions come from accounting for residual stress, slip system-level backstress, and latent hardening. We are confident to state that the advanced MS-EPSC model used in the present work can be applied to other HCP metals, deforming by multiple slip and twinning deformation mechanisms under a wide range of strain rate, temperature, and strain-path conditions.

Acknowledgements

N. C. F, Z. F., and M. K. acknowledge financial support from the U.S. National Science Foundation (NSF) under the CAREER program (CMMI-1650641).

Appendix A

Lattice strain analysis procedure performed using GSAS-II & MATLAB:

I. *CeO_2 Calibration in GSAS-II (Bright image file → Image controls)*
   1. Import bright and dark CeO2.ge2 files into GSAS-II (make sure each .ge file has the same exposure time at identical sample-to-detector distances).
   2. Enter approximate values for beam center x+y and distance.

3. Enter exact value for wavelength.
4. Refine all calibration coefficients except wavelength (and possibly penetration).
5. Select dark image file.
6. Choose CeO2 SRM674b for a calibrant.
7. Set minimum d-spacing to 0.5 or 0.4 and pixel search range to 2 (if broad peaks increase to 5).
8. Calibration → Calibrate: left click on innermost diffraction ring in 5 or 6 different places then right click to calibrate.
9. Calibrate → Recalibrate until values don't change.
10. *Save CeO_2 calibration file: Image Controls → Parms → Save Controls.*

II. *Import & Integrate Be images (GSAS-II)*

1. Import dark Be.ge2 file and all in-situ loading bright Be.ge2 files into GSAS-II (make sure each .ge file has the same exposure time at identical sample to detector distances).
2. Select first Be bright file.
3. Load CeO_2 calibration file.
    - Image controls → Parms → Load Controls: load CeO_2 calibration file.
4. Choose dark image.
5. Check "show integration limits" and "Do full integration" under integration coefficients.
6. Choose appropriate azimuth (phi) and 2Theta integration limits (in this case <u>-7.5 : 352.5</u> and 3.5 : 10.3).
7. Choose number of bins: usually 2500 for 2Theta and either 1 or 24 for azimuthal bins (in this case 24).
8. Integrate histograms.
    - Integration → Integrate all histograms.
9. Delete image files from project.

III. *Single Peak Fitting (GSAS-II)*

1. Select a pwdr data file with all peaks visible you want to analyze.
2. Peak List → Peak Fitting → AutoSearch: Manually add missing peaks and delete extra peaks.
3. Check refine box for position and intensity for all peaks. Peak Fitting → Peakfit.
4. Check refine box for sigma for all peaks. Peak Fitting → Peakfit.
5. Check refine box for gamma for all peaks. Peak Fitting → Peakfit (If this gives bad values, reset all values and repeat steps 3+4).
6. Uncheck all sigma (and gamma if that was refined) boxes. Peak fitting → SeqPeakFit (all histograms), then save project.
    - Depending on texture, sigma could possibly be refined in a second round of seq peak fitting. Gamma unlikely.

7. Export sequential data: load save with best refinement results → sequential results → Col/Rows → Save all as CSV.

IV. *Lattice Strain Analysis (MATLAB)*

1. Import load and position data from WAXS (or APS par) file and GSAS-II peak position data (including from virgin sample).
2. Convert load/position to true stress-strain and separate loading and unloading.
3. Select parallel and perpendicular planes from peak data (90º/270º and 0º/180º Φ (azimuthal axis)) and convert 2θ peak positions to d-spacing.
4. Calculate lattice strains for each peak from d-spacing data (use virgin sample as initial) and associated error.
5. Couple lattice strain data to applied stress data.
6. Save compression stress-strain data.
7. Save lattice strain data for both parallel and perpendicular planes for each peak as a function of applied stress.

Texture analysis procedure performed using MAUD, ImageJ, & MATLAB/MTEX:

I. *Initialize CeO_2 image files in ImageJ for CeO_2 Calibration*

1. Convert CeO2.ge2 files to .tiff files.
2. Load dark and bright CeO2.ge2 files into ImageJ.
   - File→Import → Raw: 16-bit unsigned, 2048x2048 pixels, 8192byte offset, little-endian byte order.
3. Subtract dark from bright (Process → ImageCalculator) and save as .tiff.

II. *Import integrated CeO_2_dkSub.tiff into Maud*

1. Import files into Maud.
   - Dataset → datafiles → fromImages. ImageJ now pops up: File → Open CeO2_dkSub.tiff.
2. Set pixel dimensions in ImageJ:
   - Image → Properties: Units=mm, pixel dims=0.2.
3. Change other image parameters in ImageJ
   - Plugins → MaudPlugins → Multi-spectraFromNormalTransmission.
   - Enter approx. sample-detector distance.
   - Find center X and Y (change circle radius to match a diffraction ring for assistance).
   - Start: 0º, end:360º (azimuthal angle, Φ), #spectra=72.
   - Click OK and save .eng file as original file name/number

III. *Manually alter diffraction instrument settings in Maud and import phase*

1. Set Incident Intensity=0.01.
2. Set Intensity Calib: non cal.

3. Set Angular Calib: Flat image transmission → set: detector dist.
4. Set Geometry: Image 2D.
5. Set Measurement: 2Theta.
6. Set Source: Synchrotron→set: wavelength.
7. Set Detector: Scintillation.
8. Set Instr Broad: Caglioti PV → set: all asym=0, HWHM 1+2=0, HWHM 3=0.0025, all Gauss=0
9. Enter computation range.
10. Add bk param if needed.
11. Import phase: CeO2.cif file.

IV. *CeO_2 Rietveld refinements to determine instrumental broadening parameters (calibration)*

1. Refine: bk, scale
2. Refine: bk, scale, angular calib (detector dist, center x, center y, tilt x, tilt y)
3. Refine: bk, scale, angular calib (detector dist, center x, center y, tilt x, tilt y), instr broad (all hwhf)
4. Refine: bk, scale, angular calib (detector dist, center x, center y, tilt x, tilt y), instr broad (all hwhf, gauss 1)
5. Refine: bk, scale, angular calib (detector dist, center x, center y, tilt x, tilt y), instr broad (all hwhf, gauss 1, gauss 2)
6. Refine: bk, scale, angular calib (detector dist, center x, center y, tilt x, tilt y), instr broad (all hwhf, gauss 1, gauss 2), arb texture
7. Refine: bk, scale, angular calib (detector dist, center x, center y, tilt x, tilt y), instr broad (all hwhf, gauss 1, gauss 2, asym 1)
8. Refine: bk, scale, angular calib (detector dist, center x, center y, tilt x, tilt y), instr broad (all hwhf, gauss 1, gauss 2, asym 1, asym 2)
   - Gauss 2, asym 1, and asym 2 may not converge, in which case do not refine.
9. Save instrument parameter file: create empty .ins file in appropriate directory, in Maud “store” instr param in that ins file

V. *Initialize Be image files in ImageJ for Texture Analysis*

1. Convert all Be.ge2 files to .tiff files
2. Load dark Be.ge2 file into ImageJ
   - File → Import → Raw: 16-bit unsigned, 2048x2048 pixels, 8192byte offset, little-endian byte order
3. Load first bright Be.ge2 file into ImageJ the same way as the dark file
4. Subtract dark from bright (Process→ImageCalculator) and save as .tiff
5. Repeat for all bright image files

VI. *Import integrated Be_dkSub.tiff files into Maud and Initialize for Texture Analysis*

1. Delete CeO_2 datafiles in dataset

2. Duplicate dataset so the number of datasets equals the number of Be files to be imported (keeps calibrated instr params for each dataset)
3. Maud: Dataset → datafiles → fromImages. ImageJ now pops up: File → Open Be_dkSub.tiff
4. Set pixel dimensions in ImageJ
    - Image → Properties: Units=mm, pixel dims=0.2
5. Change other image parameters in ImageJ
    - Plugins → MaudPlugins → Multi-spectraFromNormalTransmission
    - Enter exact sample-detector distance
    - Find center X and Y (change circle radius to match a diffraction ring for assistance)
    - Start: 0º, end: 360º (azimuthal angle, Φ), #spectra=72
    - Click OK and save .eng file as original file name/number
6. Repeat this process in new datasets for each Be file
7. Enter appropriate rotation (ω) angles for each dataset (dataset → settings → modifyAngles: ω = ##º)
8. Enter computation ranges for each dataset
9. Add bk params if needed for each dataset
10. Import phase: Be.cif file

VII. *Be Rietveld refinements to determine texture (remember to first fix all parameters before refining)*

1. Refine: bk, scale
2. Refine: bk, scale, basic (no Biso)
3. Refine: bk, scale, basic (no Biso, no lattice parameter), sample-detect dist
4. Refine: bk, scale, basic (no Biso), microstrain
5. Refine: bk, scale, basic (no Biso), microstrain, cryst size
6. Refine: bk, scale, basic (no Biso), microstrain, cryst size, texture5 (E-WIMV, 7.5deg res)
7. Refine: bk, scale, basic (no Biso), microstrain, cryst size, texture8 (E-WIMV, 7.5deg res)
8. Refine: bk, scale, basic (no Biso), microstrain, cryst size, texture10 (E-WIMV, 7.5deg res)
9. Export ODF (beartex formatted)

VIII. *Plot Pole Figures in MATLAB/MTEX*

1. Make MTEX reference frame same as MAUD
2. Convert ODF to Euler angle format and load/reconstruct using MTEX (7.5deg res, 5deg HW)
3. Rotate ODF +90º about IP2 axis and plot pole figures.

References

Abey, A., 1970. Effect of pressure and strain rate on the shear strength of beryllium. J. Appl. Phys. 41, 5254-5259.

Aldinger, F., 1979. Flow and Fracture of Single Crystals (Beryllium Crystal Dislocations), in: Webster, D., London, G.J. (Eds.), Beryllium Science and Technology. New York, NY: Plenum Press, p. 7.

Alves, J.M., Brandao, L.P., Paula, A.d.S., 2015. The influence of sample preparation on the quantitative analysis of the volume fraction of martensite formed in a 304L trip steel. Materials Research 18, 159-163.

Ardeljan, M., Beyerlein, I.J., Knezevic, M., 2014. A dislocation density based crystal plasticity finite element model: Application to a two-phase polycrystalline HCP/BCC composites. J. Mech. Phys. Solids 66, 16-31.

Ardeljan, M., Beyerlein, I.J., Knezevic, M., 2017. Effect of dislocation density-twin interactions on twin growth in AZ31 as revealed by explicit crystal plasticity finite element modeling. Int. J. Plast. 99, 81-101.

Ardeljan, M., Beyerlein, I.J., McWilliams, B.A., Knezevic, M., 2016a. Strain rate and temperature sensitive multi-level crystal plasticity model for large plastic deformation behavior: Application to AZ31 magnesium alloy. Int. J. Plast. 83, 90-109.

Ardeljan, M., Knezevic, M., 2018. Explicit modeling of double twinning in AZ31 using crystal plasticity finite elements for predicting the mechanical fields for twin variant selection and fracture analyses. Acta. Mater. 157, 339-354.

Ardeljan, M., Knezevic, M., Nizolek, T., Beyerlein, I.J., Mara, N.A., Pollock, T.M., 2015a. A study of microstructure-driven strain localizations in two-phase polycrystalline HCP/BCC composites using a multi-scale model. Int. J. Plast. 74, 35-57.

Ardeljan, M., McCabe, R.J., Beyerlein, I.J., Knezevic, M., 2015b. Explicit incorporation of deformation twins into crystal plasticity finite element models. Computer Methods in Applied Mechanics and Engineering 295, 396-413.

Ardeljan, M., Savage, D.J., Kumar, A., Beyerlein, I.J., Knezevic, M., 2016b. The plasticity of highly oriented nano-layered Zr/Nb composites. Acta. Mater. 115, 189-203.

Barrett, T.J., Eghtesad, A., McCabe, R.J., Clausen, B., Brown, D.W., Vogel, S.C., Knezevic, M., 2019. A generalized spherical harmonics-based procedure for the interpolation of partial datasets of orientation distributions to enable crystal mechanics-based simulations. Materialia 6, 100328.

Barrett, T.J., Knezevic, M., 2019. Deep drawing simulations using the finite element method embedding a multi-level crystal plasticity constitutive law: Experimental verification and sensitivity analysis. Computer Methods in Applied Mechanics and Engineering 354, 245-270.

Barrett, T.J., McCabe, R.J., Brown, D.W., Clausen, B., Vogel, S.C., Knezevic, M., 2020. Predicting deformation behavior of α-uranium during tension, compression, load reversal, rolling, and sheet forming using elasto-plastic, multi-level crystal plasticity coupled with finite elements. J. Mech. Phys. Solids 138, 103924.

Bertin, N., Tomé, C.N., Beyerlein, I.J., Barnett, M.R., Capolungo, L., 2014. On the strength of dislocation interactions and their effect on latent hardening in pure Magnesium. Int. J. Plast. 62, 72-92.

Beyerlein, I.J., Tomé, C.N., 2008. A dislocation-based constitutive law for pure Zr including temperature effects. Int. J. Plast. 24, 867-895.

Beyerlein, I.J., Zhang, X., Misra, A., 2014. Growth Twins and Deformation Twins in Metals. Annual Review of Materials Research 44, 329-363.
Bhattacharyya, J.J., Wang, F., Wu, P.D., Whittington, W.R., El Kadiri, H., Agnew, S.R., 2016. Demonstration of alloying, thermal activation, and latent hardening effects on quasi-static and dynamic polycrystal plasticity of Mg alloy, WE43-T5, plate. Int. J. Plast. 81, 123-151.
Blumenthal, W., Brown, D., Tomé, C., 2004. Evolution of crystallographic texture and strength in beryllium, AIP conference proceedings. American Institute of Physics, pp. 525-528.
Bourke, M., Dunand, D., Ustundag, E., 2002. SMARTS–a spectrometer for strain measurement in engineering materials. Applied Physics A 74, s1707-s1709.
Brown, D., Abeln, S., Blumenthal, W., Bourke, M., Mataya, M., Tome, C., 2005a. Development of crystallographic texture during high rate deformation of rolled and hot-pressed beryllium. Metall. Mater. Trans. A 36, 929-939.
Brown, D., Bourke, M., Tomé, C., Varma, R., Holden, T., Clausen, B., 2003. A neutron diffraction and modeling study of uniaxial deformation in polycrystalline beryllium. Metall. Mater. Trans. A 34, 1439-1449.
Brown, D.W., Agnew, S.R., Abeln, S., Blumenthal, W., Bourke, M.A., Mataya, M., Tomé, C., Vogel, S.C., 2005b. The role of texture, temperature and strain rate in the activity of deformation twinning, Materials Science Forum. Trans Tech Publ, pp. 1037-1042.
Brown, D.W., Almer, J.D., Clausen, B., Mosbrucker, P.L., Sisneros, T.A., Vogel, S.C., 2013. Twinning and de-twinning in beryllium during strain path changes. Mater. Sci. Eng. A 559, 29-39.
Brown, D.W., Beyerlein, I.J., Sisneros, T.A., Clausen, B., Tomé, C.N., 2012. Role of twinning and slip during compressive deformation of beryllium as a function of strain rate. Int. J. Plast. 29, 120-135.
Chen, S.R., Kocks, U.F., 1991. High-Temperature Plasticity in Copper Polycrystals, High Temperature Constitutive Modeling - Theory and Application, A.D. Freed and K.P. Walker, eds., Atlanta, GA, The American Society of Mechanical Engineers, pp. 1-12.
Chin, G.Y., Mamme, W.L., 1969. Generalization and Equivalence of the Minimum Work (Taylor) and Maximum Work (Bishop-Hill) Principles for Crystal Plasticity. Transactions of the Metallurgical Society of AIME 245, 1211-1214.
Christian, J.W., Mahajan, S., 1995. Deformation twinning. Prog. Mater. Sci. 39, 1-157.
Clausen, B., Tomé, C.N., Brown, D.W., Agnew, S.R., 2008. Reorientation and stress relaxation due to twinning: Modeling and experimental characterization for Mg. Acta. Mater. 56, 2456-2468.
Eghtesad, A., Barrett, T.J., Germaschewski, K., Lebensohn, R.A., McCabe, R.J., Knezevic, M., 2018a. OpenMP and MPI implementations of an elasto-viscoplastic fast Fourier transform-based micromechanical solver for fast crystal plasticity modeling. Advances in Engineering Software 126, 46-60.
Eghtesad, A., Barrett, T.J., Knezevic, M., 2018b. Compact reconstruction of orientation distributions using generalized spherical harmonics to advance large-scale crystal plasticity modeling: Verification using cubic, hexagonal, and orthorhombic polycrystals. Acta. Mater. 155, 418-432.
Eghtesad, A., Germaschewski, K., Beyerlein, I.J., Hunter, A., Knezevic, M., 2018c. Graphics processing unit accelerated phase field dislocation dynamics: Application to bi-metallic interfaces. Advances in Engineering Software 115, 248-267.

Eghtesad, A., Germaschewski, K., Lebensohn, R.A., Knezevic, M., 2020. A multi-GPU implementation of a full-field crystal plasticity solver for efficient modeling of high-resolution microstructures. Computer Physics Communications, 107231.
Eghtesad, A., Knezevic, M., 2018. A new approach to fluid–structure interaction within graphics hardware accelerated smooth particle hydrodynamics considering heterogeneous particle size distribution. Computational Particle Mechanics 5, 387-409.
Eghtesad, A., Knezevic, M., 2020a. A full-field crystal plasticity model including the effects of precipitates: Application to monotonic, load reversal, and low-cycle fatigue behavior of Inconel 718. Mater. Sci. Eng. A, 140478.
Eghtesad, A., Knezevic, M., 2020b. High-performance full-field crystal plasticity with dislocation-based hardening and slip system back-stress laws: Application to modeling deformation of dual-phase steels. J. Mech. Phys. Solids 134, 103750.
Eghtesad, A., Knezevic, M., 2021. Modeling cyclic plasticity of additively manufactured alloy Mar-M-509 using a high-performance spectral-based micromechanical model. Applications in Engineering Science 7, 100065.
Eghtesad, A., Zecevic, M., Lebensohn, R.A., McCabe, R.J., Knezevic, M., 2018d. Spectral database constitutive representation within a spectral micromechanical solver for computationally efficient polycrystal plasticity modelling. Comput. Mech. 61, 89-104.
Eshelby, J.D., 1957. The determination of the elastic field of an ellipsoidal inclusion, and related problems. Proc R. Soc. Lond. A 241, 376-396.
Feather, W.G., Ghorbanpour, S., Savage, D.J., Ardeljan, M., Jahedi, M., McWilliams, B.A., Gupta, N., Xiang, C., Vogel, S.C., Knezevic, M., 2019. Mechanical response, twinning, and texture evolution of WE43 magnesium-rare earth alloy as a function of strain rate: Experiments and multi-level crystal plasticity modeling. Int. J. Plast. 120, 180-204.
Feather, W.G., Savage, D.J., Knezevic, M., 2021. A crystal plasticity finite element model embedding strain-rate sensitivities inherent to deformation mechanisms: Application to alloy AZ31. Int. J. Plast. 143, 103031.
Feng, Z., Yoon, S.-Y., Choi, J.-H., Barrett, T.J., Zecevic, M., Barlat, F., Knezevic, M., 2020. A comparative study between elasto-plastic self-consistent crystal plasticity and anisotropic yield function with distortional hardening formulations for sheet metal forming. Mechanics of Materials 148, 103422.
Feng, Z., Zecevic, M., Knezevic, M., 2021. Stress-assisted ($\gamma \rightarrow \alpha'$) and strain-induced ($\gamma \rightarrow \varepsilon \rightarrow \alpha'$) phase transformation kinetics laws implemented in a crystal plasticity model for predicting strain path sensitive deformation of austenitic steels. Int. J. Plast. 136, 102807.
Follansbee, P.S., 1985. High Strain Rate Compression Testing - The Hopkinson Bar. 9th edn. Vol. 8, Am. Soc. Metals, Metals Park, Ohio, pp. 198-203.
Fromm, B.S., Adams, B.L., Ahmadi, S., Knezevic, M., 2009. Grain size and orientation distributions: Application to yielding of α-titanium. Acta. Mater. 57, 2339-2348.
Ghorbanpour, S., Alam, M.E., Ferreri, N.C., Kumar, A., McWilliams, B.A., Vogel, S.C., Bicknell, J., Beyerlein, I.J., Knezevic, M., 2020. Experimental characterization and crystal plasticity modeling of anisotropy, tension-compression asymmetry, and texture evolution of additively manufactured Inconel 718 at room and elevated temperatures. Int. J. Plast. 125, 63-79.
Ghorbanpour, S., Zecevic, M., Kumar, A., Jahedi, M., Bicknell, J., Jorgensen, L., Beyerlein, I.J., Knezevic, M., 2017. A crystal plasticity model incorporating the effects of precipitates in

superalloys: Application to tensile, compressive, and cyclic deformation of Inconel 718. Int. J. Plast. 99, 162-185.
Harder, J., 1999. A crystallographic model for the study of local deformation processes in polycrystals. Int. J. Plast. 15, 605-624.
Jain, A., Agnew, S.R., 2007. Modeling the temperature dependent effect of twinning on the behavior of Mg alloy AZ31 sheet. Mater. Sci. Eng. A, 29-36.
Jeong, Y., Jeon, B., Tomé, C.N., 2021. Finite element analysis using an incremental elasto-visco-plastic self-consistent polycrystal model: FE simulations on Zr and low-carbon steel subjected to bending, stress-relaxation, and unloading. Int. J. Plast. 147, 103110.
Jonsson, S., Beuers, J., 1987. The dislocation structure in beryllium single crystals deformed by prismatic slip. Materials Science and Engineering 91, 111-123.
Kaiser, D., Watters Jr, R., 2007. SRM 674b x-ray powder diffraction intensity set for quantitative analysis by x-ray powder diffraction. National Institute of Standards and Technology, US Department of Commerce, Gaithersburg 970.
Kalidindi, S.R., 1998. Incorporation of deformation twinning in crystal plasticity models. J. Mech. Phys. Solids 46, 267-271.
Kalidindi, S.R., Bronkhorst, C.A., Anand, L., 1992. Crystallographic texture evolution in bulk deformation processing of FCC metals. J. Mech. Phys. Solids 40, 537-569.
Kassner, M.E., Geantil, P., Levine, L.E., 2013. Long range internal stresses in single-phase crystalline materials. International Journal of Plasticity 45, 44-60.
Khadyko, M., Dumoulin, S., Cailletaud, G., Hopperstad, O.S., 2016. Latent hardening and plastic anisotropy evolution in AA6060 aluminium alloy. Int. J. Plast. 76, 51-74.
Kitayama, K., Tomé, C., Rauch, E., Gracio, J., Barlat, F., 2013a. A crystallographic dislocation model for describing hardening of polycrystals during strain path changes. Application to low carbon steels. Int. J. Plast. 46, 54-69.
Kitayama, K., Tomé, C.N., Rauch, E.F., Gracio, J.J., Barlat, F., 2013b. A crystallographic dislocation model for describing hardening of polycrystals during strain path changes. Application to low carbon steels. International Journal of Plasticity 46, 54-69.
Knezevic, M., Al-Harbi, H.F., Kalidindi, S.R., 2009. Crystal plasticity simulations using discrete Fourier transforms. Acta. Mater. 57, 1777-1784.
Knezevic, M., Beyerlein, I.J., Brown, D.W., Sisneros, T.A., Tomé, C.N., 2013a. A polycrystal plasticity model for predicting mechanical response and texture evolution during strain-path changes: Application to beryllium. Int. J. Plast. 49, 185-198.
Knezevic, M., Daymond, M.R., Beyerlein, I.J., 2016a. Modeling discrete twin lamellae in a microstructural framework. Scr. Mater. 121, 84-88.
Knezevic, M., Drach, B., Ardeljan, M., Beyerlein, I.J., 2014. Three dimensional predictions of grain scale plasticity and grain boundaries using crystal plasticity finite element models. Computer Methods in Applied Mechanics and Engineering 277, 239-259.
Knezevic, M., Kalidindi, S.R., Fullwood, D., 2008. Computationally efficient database and spectral interpolation for fully plastic Taylor-type crystal plasticity calculations of face-centered cubic polycrystals. Int. J. Plast. 24, 1264-1276.
Knezevic, M., Landry, N.W., 2015. Procedures for reducing large datasets of crystal orientations using generalized spherical harmonics. Mechanics of Materials 88, 73-86.
Knezevic, M., Lebensohn, R.A., Cazacu, O., Revil-Baudard, B., Proust, G., Vogel, S.C., Nixon, M.E., 2013b. Modeling bending of α-titanium with embedded polycrystal plasticity in implicit finite elements. Mater. Sci. Eng. A 564, 116-126.

Knezevic, M., Levinson, A., Harris, R., Mishra, R.K., Doherty, R.D., Kalidindi, S.R., 2010. Deformation twinning in AZ31: Influence on strain hardening and texture evolution. Acta. Mater. 58, 6230-6242.
Knezevic, M., McCabe, R.J., Lebensohn, R.A., Tomé, C.N., Liu, C., Lovato, M.L., Mihaila, B., 2013c. Integration of self-consistent polycrystal plasticity with dislocation density based hardening laws within an implicit finite element framework: Application to low-symmetry metals. J. Mech. Phys. Solids 61, 2034-2046.
Knezevic, M., Savage, D.J., 2014. A high-performance computational framework for fast crystal plasticity simulations. Comput. Mater. Sci. 83, 101-106.
Knezevic, M., Zecevic, M., Beyerlein, I.J., Bingert, J.F., McCabe, R.J., 2015. Strain rate and temperature effects on the selection of primary and secondary slip and twinning systems in HCP Zr. Acta. Mater. 88, 55-73.
Knezevic, M., Zecevic, M., Beyerlein, I.J., Lebensohn, R.A., 2016b. A numerical procedure enabling accurate descriptions of strain rate-sensitive flow of polycrystals within crystal visco-plasticity theory. Computer Methods in Applied Mechanics and Engineering 308, 468-482.
Kocks, U.F., Franciosi, P., Kawai, M., 1991. A Forest Model of Latent Hardening and its Application to Polycrystal Deformations. Textures and Microstructures 14, 1103-1114.
Kocks, U.F., Mecking, H., 1981. Kinetics of Flow and Strain-Hardening. Acta Metall. 29, 1865-1875.
Kocks, U.F., Tomé, C.N., Wenk, H.-R., 1998. Texture and Anisotropy. Cambridge University Press, Cambridge, UK.
Kokovikhin, Y.I., Roraanko, P., Lashchuk, N., Krivko, V., Baryshnikova, S., 1990. Temperature-rate dependence of the mechanical properties of commercial-grade beryllium. Strength of materials 22, 1616-1619.
Lavrentev, F.F., 1980. The type of dislocation interaction as the factor determining work hardening. Materials Science and Engineering 46, 191-208.
Lebensohn, R.A., Kanjarla, A.K., Eisenlohr, P., 2012. An elasto-viscoplastic formulation based on fast Fourier transforms for the prediction of micromechanical fields in polycrystalline materials. Int. J. Plast. 32-33, 59-69.
Lebensohn, R.A., Tomé, C.N., 1993. A self-consistent anisotropic approach for the simulation of plastic deformation and texture development of polycrystals: Application to zirconium alloys. Acta Metall. Mater. 41, 2611-2624.
Lebensohn, R.A., Zecevic, M., Knezevic, M., McCabe, R.J., 2016. Average intragranular misorientation trends in polycrystalline materials predicted by a viscoplastic self-consistent approach. Acta. Mater. 104, 228-236.
Lipinski, P., Berveiller, M., 1989. Elastoplasticity of micro-inhomogeneous metals at large strains. Int. J. Plast. 5, 149-172.
Mahesh, S., Tomé, C.N., McCabe, R.J., Kaschner, G.C., Misra, A., Beyerlein, I.J., 2004. Application of a substructure-based hardening model to copper under loading path changes. Metall. Mater. Trans. A 35, 3763-3774.
Matthies, S., Lutteroti, L., Wenk, H., 1997. Advances in texture analysis from diffraction spectra. Journal of Applied Crystallography 30, 31-42.
Mughrabi, H., 1983. Dislocation wall and cell structures and long-range internal stresses in deformed metal crystals. Acta Metall. 31, 1367-1379.

Neil, C.J., Wollmershauser, J.A., Clausen, B., Tomé, C.N., Agnew, S.R., 2010. Modeling lattice strain evolution at finite strains and experimental verification for copper and stainless steel using in situ neutron diffraction. Int. J. Plast. 26, 1772-1791.
Niezgoda, S.R., Kanjarla, A.K., Beyerlein, I.J., Tomé, C.N., 2014. Stochastic modeling of twin nucleation in polycrystals: An application in hexagonal close-packed metals. Int. J. Plast. 56, 119-138.
Panchal, J.H., Kalidindi, S.R., McDowell, D.L., 2013. Key computational modeling issues in Integrated Computational Materials Engineering. Computer-Aided Design 45, 4-25.
Partiridge, P.G., 1967. The crystallography and deformation modes of hexagonal close-packed metals. Metallurgia Revised 12, 169.
Partridge, P.G., Roberts, E., 1964. The formation and behaviour of incoherent twin boundaries in hexagonal metals. Acta Metall. 12, 1205-1210.
Peeters, B., Seefeldt, M., Teodosiu, C., Kalidindi, S.R., Van Houtte, P., Aernoudt, E., 2001. Work-hardening/softening behaviour of b.c.c. polycrystals during changing strain paths: I. An integrated model based on substructure and texture evolution, and its prediction of the stress-strain behaviour of an IF steel during two-stage strain paths. Acta. Mater. 49, 1607-1619.
Poirier, J.P., Antolin, J., Dupouy, J.M., 1967. Investigations on some deformation modes of beryllium. Canadian Journal of Physics 45, 1221-1224.
Poulsen, H.F., 2004. Three-dimensional X-ray diffraction microscopy: mapping polycrystals and their dynamics. Springer Science & Business Media.
Prakash, A., Nöhring, W.G., Lebensohn, R.A., Höppel, H.W., Bitzek, E., 2015. A multiscale simulation framework of the accumulative roll bonding process accounting for texture evolution. Mater. Sci. Eng. A 631, 104-119.
Proust, G., Kaschner, G.C., Beyerlein, I.J., Clausen, B., Brown, D.W., McCabe, R.J., Tomé, C.N., 2010. Detwinning of High-Purity Zirconium: In-Situ Neutron Diffraction Experiments. Experimental Mechanics 50, 125-133.
Proust, G., Tomé, C.N., Kaschner, G.C., 2007. Modeling texture, twinning and hardening evolution during deformation of hexagonal materials. Acta. Mater. 55, 2137-2148.
Rauch, E., Gracio, J., Barlat, F., Vincze, G., 2011. Modelling the plastic behaviour of metals under complex loading conditions. Modelling and Simulation in Materials Science and Engineering 19, 1-18.
Risse, M., Lentz, M., Fahrenson, C., Reimers, W., Knezevic, M., Beyerlein, I.J., 2017. Elevated Temperature Effects on the Plastic Anisotropy of an Extruded Mg-4 Wt Pct Li Alloy: Experiments and Polycrystal Modeling. Metall. Mater. Trans. A 48, 446-458.
Roters, F., Eisenlohr, P., Hantcherli, L., Tjahjanto, D.D., Bieler, T.R., Raabe, D., 2010. Overview of constitutive laws, kinematics, homogenization and multiscale methods in crystal plasticity finite-element modeling: Theory, experiments, applications. Acta. Mater. 58, 1152-1211.
Savage, D.J., Beyerlein, I.J., Mara, N.A., Vogel, S.C., McCabe, R.J., Knezevic, M., 2019. Microstructure and texture evolution in Mg/Nb layered materials made by accumulative roll bonding. Int. J. Plast.
Savage, D.J., Feng, Z., Knezevic, M., 2021. Identification of crystal plasticity model parameters by multi-objective optimization integrating microstructural evolution and mechanical data. Computer Methods in Applied Mechanics and Engineering 379, 113747.

Segurado, J., Lebensohn, R.A., Llorca, J., Tomé, C.N., 2012. Multiscale modeling of plasticity based on embedding the viscoplastic self-consistent formulation in implicit finite elements. Int. J. Plast. 28, 124-140.
Shade, P.A., Musinski, W.D., Obstalecki, M., Pagan, D.C., Beaudoin, A.J., Bernier, J.V., Turner, T.J., 2019. Exploring new links between crystal plasticity models and high-energy X-ray diffraction microscopy. Current Opinion in Solid State and Materials Science 23, 100763.
Shastri, S.D., Fezzaa, K., Mashayekhi, A., Lee, W.K., Fernandez, P.B., Lee, P.L., 2002. Cryogenically cooled bent double-Laue monochromator for high-energy undulator X-rays (50-200 keV). J. Syncrotron Rad. 9, 317-322.
Sisneros, T.A., Brown, D.W., Clausen, B., Donati, D.C., Kabra, S., Blumenthal, W.R., Vogel, S.C., 2010. Influence of strain rate on mechanical properties and deformation texture of hot-pressed and rolled beryllium. Mater. Sci. Eng. A 527, 5181-5188.
Song, S., Gray, G., 1995. Influence of temperature and strain rate on slip and twinning behavior of Zr. Metall. Mater. Trans. A 26, 2665-2675.
Tam, K.J., Vaughan, M.W., Shen, L., Knezevic, M., Karaman, I., Proust, G., 2020. Modelling the temperature and texture effects on the deformation mechanisms of magnesium alloy AZ31. International Journal of Mechanical Sciences 182, 105727.
Tam, K.J., Vaughan, M.W., Shen, L., Knezevic, M., Karaman, I., Proust, G., 2021. Modelling dynamic recrystallisation in magnesium alloy AZ31. Int. J. Plast. 142, 102995.
Taylor, G.I., 1938. Plastic strain in metals. Journal of the Institute of Metals 62, 307-324.
Teodosiu, C., Raphanel, J.L., 1991. Finite element simulations of large elastoplastic deformations of multicrystals. Proceedings of the International Seminar MECAMAT91, 153-168.
Toby, B.H., Von Dreele, R.B., 2013. GSAS-II: the genesis of a modern open-source all purpose crystallography software package. Journal of Applied Crystallography 46, 544-549.
Tomé, C.N., 1999. Self-consistent polycrystal models: A directional compliance criterion to describe grain interactions. Modelling and Simulation in Materials Science and Engineering 7, 723-738.
Tomé, C.N., Lebensohn, R.A., Kocks, U.F., 1991. A model for texture development dominated by deformation twinning: Application to zirconium alloys. Acta Metall. Mater. 39, 2667-2680.
Tomé, C.N., Maudlin, P.J., Lebensohn, R.A., Kaschner, G.C., 2001. Mechanical response of zirconium: I. Derivation of a polycrystal constitutive law and finite element analysis. Acta. Mater. 49, 3085-3096.
Turner, P.A., Tomé, C.N., 1994. A study of residual stresses in Zircaloy-2 with rod texture. Acta Metall. Mater. 42, 4143-4153.
Van Houtte, P., 1978. Simulation of the rolling and shear texture of brass by the Taylor theory adapted for mechanical twinning. Acta Metall. Mater. 26, 591-604.
Walde, T., Riedel, H., 2007. Simulation of earing during deep drawing of magnesium alloy AZ31. Acta. Mater. 55, 867-874.
Wang, H., Wu, P.D., Tomé, C.N., Wang, J., 2012. A constitutive model of twinning and detwinning for hexagonal close packed polycrystals. Mater. Sci. Eng. A 555, 93-98.
Wang, L., Lind, J., Phukan, H., Kenesei, P., Park, J.-S., Suter, R., Beaudoin, A., Bieler, T., 2014. Mechanical twinning and detwinning in pure Ti during loading and unloading–An in situ high-energy X-ray diffraction microscopy study. Scr. Mater. 92, 35-38.

Wen, W., Borodachenkova, M., Tomé, C., Vincze, G., Rauch, E., Barlat, F., Grácio, J., 2015a. Mechanical behavior of Mg subjected to strain path changes: Experiments and modeling. Int. J. Plast. 73, 171-183.
Wen, W., Borodachenkova, M., Tomé, C.N., Vincze, G., Rauch, E.F., Barlat, F., Grácio, J.J., 2015b. Mechanical behavior of Mg subjected to strain path changes: Experiments and modeling. International Journal of Plasticity 73, 171-183.
Wen, W., Borodachenkova, M., Tomé, C.N., Vincze, G., Rauch, E.F., Barlat, F., Grácio, J.J., 2016. Mechanical behavior of low carbon steel subjected to strain path changes: Experiments and modeling. Acta. Mater. 111, 305-314.
Wenk, H.-R., Lutterotti, L., Vogel, S., 2003. Texture analysis with the new HIPPO TOF diffractometer. Nuclear Instruments and Methods in Physics Research Section A: Accelerators, Spectrometers, Detectors and Associated Equipment 515, 575-588.
Wenk, H.-R., Lutterotti, L., Vogel, S., 2010. Rietveld texture analysis from TOF neutron diffraction data. Powder Diffraction 25, 283-296.
Wilson, D.V., Bate, P.S., 1986. Reversibility in the work hardening of spheroidised steels. Acta Metall. 34, 1107-1120.
Withers, P.J., Bhadeshia, H.K.D.H., 2001. Residual stress. Part 1 – Measurement techniques. Materials Science and Technology 17, 355-365.
Wollmershauser, J.A., Clausen, B., Agnew, S.R., 2012. A slip system-based kinematic hardening model application to in situ neutron diffraction of cyclic deformation of austenitic stainless steel. Int. J. Fatigue 36, 181-193.
Yoo, M.H., 1981. Slip, twinning, and fracture in hexagonal close-packed metals. Metall. Mater. Trans. A 12, 409–418.
Zecevic, M., Beyerlein, I.J., McCabe, R.J., McWilliams, B.A., Knezevic, M., 2016a. Transitioning rate sensitivities across multiple length scales: Microstructure-property relationships in the Taylor cylinder impact test on zirconium. Int. J. Plast. 84, 138-159.
Zecevic, M., Knezevic, M., 2015. A dislocation density based elasto-plastic self-consistent model for the prediction of cyclic deformation: Application to Al6022-T4. Int. J. Plast. 72, 200-217.
Zecevic, M., Knezevic, M., 2018a. Latent hardening within the elasto-plastic self-consistent polycrystal homogenization to enable the prediction of anisotropy of AA6022-T4 sheets. Int. J. Plast. 105, 141-163.
Zecevic, M., Knezevic, M., 2018b. A new visco-plastic self-consistent formulation implicit in dislocation-based hardening within implicit finite elements: Application to high strain rate and impact deformation of tantalum. Computer Methods in Applied Mechanics and Engineering 341, 888-916.
Zecevic, M., Knezevic, M., 2019. An implicit formulation of the elasto-plastic self-consistent polycrystal plasticity model and its implementation in implicit finite elements. Mechanics of Materials 136, 103065.
Zecevic, M., Knezevic, M., Beyerlein, I.J., Tomé, C.N., 2015. An elasto-plastic self-consistent model with hardening based on dislocation density, twinning and de-twinning: Application to strain path changes in HCP metals. Mater. Sci. Eng. A 638, 262-274.
Zecevic, M., Knezevic, M., McWilliams, B., Lebensohn, R.A., 2020. Modeling of the thermo-mechanical response and texture evolution of WE43 Mg alloy in the dynamic recrystallization regime using a viscoplastic self-consistent formulation. Int. J. Plast. 130, 102705.

Zecevic, M., Korkolis, Y.P., Kuwabara, T., Knezevic, M., 2016b. Dual-phase steel sheets under cyclic tension–compression to large strains: Experiments and crystal plasticity modeling. J. Mech. Phys. Solids 96, 65-87.
Zecevic, M., Lebensohn, R.A., McCabe, R.J., Knezevic, M., 2018. Modeling of intragranular misorientation and grain fragmentation in polycrystalline materials using the viscoplastic self-consistent formulation. Int. J. Plast. 109, 193-211.
Zecevic, M., Lebensohn, R.A., McCabe, R.J., Knezevic, M., 2019a. Modelling recrystallization textures driven by intragranular fluctuations implemented in the viscoplastic self-consistent formulation. Acta. Mater. 164, 530-546.
Zecevic, M., Lebensohn, R.A., Rogers, M., Moore, J., Chiravalle, V., Lieberman, E., Dunning, D., Shipman, G., Knezevic, M., Morgan, N., 2021. Viscoplastic self-consistent formulation as generalized material model for solid mechanics applications. Applications in Engineering Science 6, 100040.
Zecevic, M., Pantleon, W., Lebensohn, R.A., McCabe, R.J., Knezevic, M., 2017. Predicting intragranular misorientation distributions in polycrystalline metals using the viscoplastic self-consistent formulation. Acta. Mater. 140, 398-410.
Zecevic, M., Upadhyay, M.V., Polatidis, E., Panzner, T., Van Swygenhoven, H., Knezevic, M., 2019b. A crystallographic extension to the Olson-Cohen model for predicting strain path dependence of martensitic transformation. Acta. Mater. 166, 386-401.